 doi:10.20944/preprints202110.0178.v1

Article

Assessment of the Contribution of a Thermodynamic and Mechanical Destabilization of Myosin–Binding Protein C Domain C2 to the Pathomechanism of Hypertrophic Cardiomyopathy–causing Double Mutation *MYBPC3*$^{\Delta 25bp/D389V}$

Frederic V. Schwäbe [1], Emanuel K. Peter[1], Manuel H. Taft[1] and Dietmar J. Manstein[1,2,3]*

[1] Institute for Biophysical Chemistry, Hannover Medical School, Fritz Hartmann Centre for Medical Research Carl Neuberg Str. 1, D-30625 Hannover, Germany; [1] Schwaebe.Frederic@mh-hannover.de (F.V.S); Peter.Emanuel@mh-hannover.de (E.K.P.); Taft.Manuel@mh-hannover.de (M.H.T.)
[2] Division for Structural Biochemistry, Hannover Medical School, Carl Neuberg Str. 1, D-30625 Hannover, Germany
[3] RESiST, Cluster of Excellence 2155, Medizinische Hochschule Hannover, D-30625 Hannover, Germany
* Correspondence: Manstein.Dietmar@mh-hannover.de

Abstract: Cardiac myosin-binding protein C (MyBPC) is a thick-filament associated regulatory protein in the sarcomere. It regulates the sensitive contractile system of the myocardium by acting as a mechanical tether, sensitizing the thin filament or modulating myosin motor activity. Mutations in the *MYBPC3* gene are a frequent cause for the development of hypertrophic cardiomyopathy, the most frequent cardiac disorder. Recently, the monoallelic double mutation *MYBPC3*$^{\Delta 25bp/D389V}$ has been discovered as a subset of the common *MYBPC3*$^{\Delta 25bp}$ variant in South Asia. *MYBPC3*$^{\Delta 25bp/D389V}$ carriers exhibit hyperdynamic features, which are considered an early finding for the development of hypertrophic cardiomyopathy. Using correlation-guided molecular dynamics simulations sampling, we show that the D389V mutation shifts the conformational distribution of the C2 domain of MyBPC. We further applied biochemical approaches to probe the effects of the D389V mutation on structure, thermostability and protein-protein interactions of MyBPC C2. The melting temperature (T_m) of MyBPC C2 D389V is decreased by 4 to 7 °C compared to wild type while the interaction of the C0-C2 domains with myosin and actin remains unchanged. Additionally, we utilized steered molecular dynamics (SMD) simulations to investigate the altered unfolding pathway of MyBPC C2 D389V. Based on our data, we propose a pathomechanism for the development of HCM in *MYBPC3*$^{\Delta 25bp}$ and *MYBPC3*$^{\Delta 25bp/D389V}$ carriers.

Keywords: cardiac muscle, cardiac contractility, force generation, enhanced molecular dynamics simulations, allostery, protein folding, disease, hypertrophic cardiomyopathy

1. Introduction

Hypertrophic cardiomyopathy (HCM) is the most frequent genetic cardiac disorder [1–4]. It is mainly characterized by an increased left ventricular wall thickness and myocyte disarray [5]. The clinical implications vary widely from no symptoms over shortness of breath to a sudden cardiac death at young age. This is partly due to the fact, that the disease can be caused by more than 1400 mutations in at least 11 different genes with *MYBPC3* and *MYH7* being the most prevalent with about 70–80% of the cases [2,6,7].

Mutations in sarcomeric genes often perturb the carefully regulated interplay of thick myosin and thin actin filaments, which is essential for cardiac function. During contraction, myosin periodically interacts with actin in a Ca^{2+}-dependent manner, which is mediated by the thin filament proteins tropomyosin and the troponin complex. In addition, the thick-filament associated cardiac myosin-binding protein C (MyBPC) takes over versatile regulatory tasks. Cardiac MyBPC (encoded by the gene *MYBPC3*) is one of three isoforms,

Preprints (www.preprints.org) | NOT PEER-REVIEWED | Posted: 12 October 2021 doi:10.20944/preprints202110.0178.v1

alongside its slow (*MYBPC1*) and fast (*MYBPC2*) counterparts in skeletal muscle. MyBPC is a modular protein of 140 kDa that comprises eight IgI-like, three FnIII-like and one unique M domain (Figure 1A). The M domain harbors multiple phosphorylation sites that modulate protein-protein interaction and are implicated in cardiac disease (as reviewed by [8,9]). MyBPC is anchored to the thick filament via its C-terminal C8-C10 domains [10–12], while its N-terminal domains interact with actin and different myosin subdomains [13–20]. Binding to myosin S2 has been demonstrated to promote myosin's super-relaxed state, limiting the number of heads accessible for contraction [21–23]. Its interaction with cardiac thin filaments (cTF) is thought to sensitize the sarcomere for Ca^{2+} by azimuthally displacing tropomyosin [24,25]. Moreover, it can apply a viscous load by tethering the thick and the thin filament, thus acting as a brake to cardiac contraction with precisely defined mechanochemical properties [26–28].

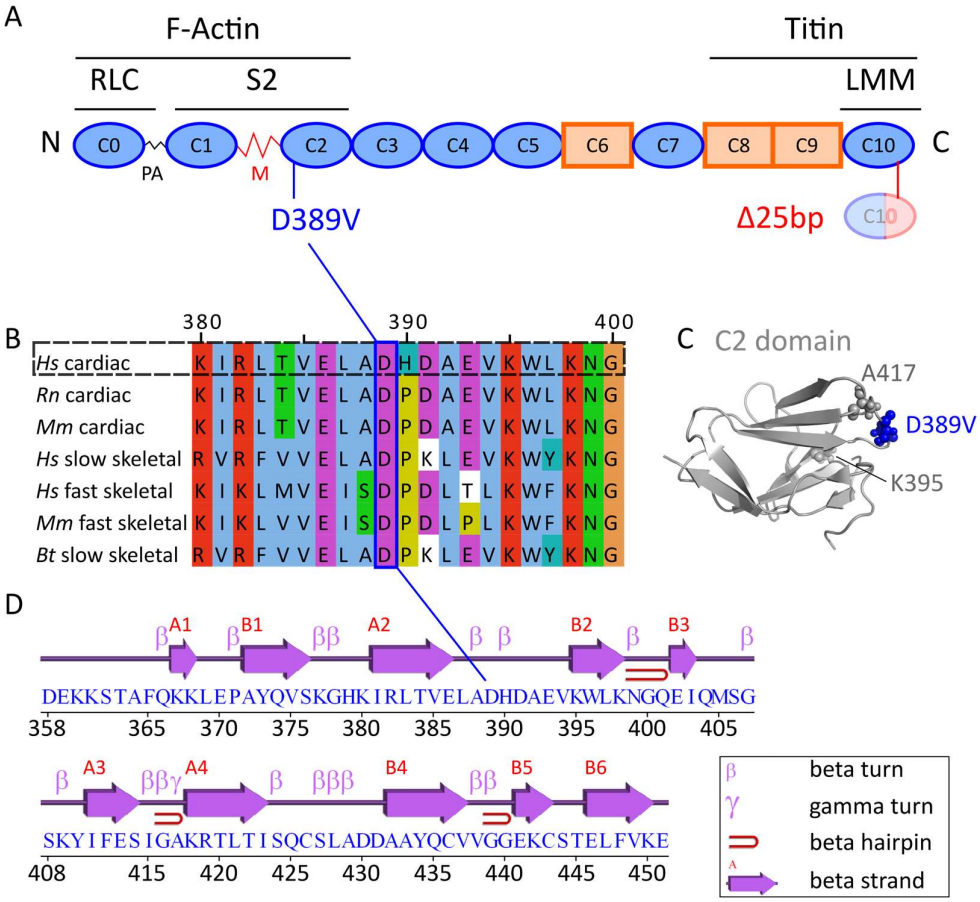

Figure 1. Schematic diagram showing the domain organization of MyBPC and its C2 domain (**A**) MyBPC consists of eight IgI-like (blue), three FnIII-like (orange) and one unique M domain. Binding partners are indicated above the respective subdomains. The positions of the *MYBPC3*$^{\Delta 25bp/D389V}$ mutation are indicated. PA: proline-alanine-rich region (**B**) Alignment of MyBPC C2 protein sequences. Residue D389 is conserved highly conserved across different mammalian isoforms. Rn: *Rattus norvegicus*, Mm: *Mus musculus*, Hs: *Homo sapiens*, Bt: *Bos Taurus* Alignment was created using T-Coffee [29] and Jalview [30]. (**C**) Cartoon representation of the MyBPC C2 domain (PDB: 5k6p [31]) with relevant residues D389, K395 and A417 displayed as spheres. (**D**) Domain topology scheme of the MYBPC C2 domain as generated using the web-based service at EMBL-EBI PDBsum (http://www.ebi.ac.uk/thornton-srv/databases/cgi-bin/pdbsum). A1–A4 and B1–B6 represent strands of the β–sheets A and B.

The majority of pathogenic *MYBPC3* mutations result in the production of a truncated protein, inducing HCM through a reduced amount of functional MyBPC (haploin-

Preprints (www.preprints.org) | NOT PEER-REVIEWED | Posted: 12 October 2021 doi:10.20944/preprints202110.0178.v1

sufficiency) [32–37]. In contrast, single amino acid replacements often destabilize a subdomain or alter protein–protein interactions, promoting development of HCM via a poison polypeptide mechanism [32,38–42].

The common *MYBPC3*$^{\Delta 25bp}$ variant with a 25 base pair intron deletion in intron 32 has been associated with an increased odds ratio of 6.99 for the development of HCM, affecting an estimated 100 million carriers in the South Asian population [43–45]. These studies showed that transcripts originating from the affected allele are subject to alternative splicing mechanisms that lead to skipping of exon 33. The resulting protein has a C10 domain with 62 residues removed and 55 added, mislocalizes to the Z–disc and its overexpression is sufficient to cause HCM in transgenic mice [46,47]. However, the probability of the alternative splicing event in human and the resulting amount of mutant protein remains unclear.

More recently, the D389V mutation in the C2 domain was discovered in ~10% of the *MYBPC3*$^{\Delta 25bp}$ carriers, constituting the monoallelic *MYBPC3*$^{\Delta 25bp/D389V}$ double mutation [48]. Individuals carrying this mutation exhibit increased left ventricular ejection fraction (LVEF), left ventricular fractional shortening (LVFS) and cardiomyocyte hypertrophy—features that are not observed in the *MYBPC3*$^{\Delta 25bp}$ cohort and that are considered early findings of HCM.

While many previous studies utilized C0–C2 or C1–C2 constructs [13–20], little is known about the biochemical properties of the C2 domain. Since *MYBPC3*$^{\Delta 25bp}$ alone is not a penetrant factor for development of HCM and has been characterized before [45–48], this study focuses on the impact of the D389V mutation in the C2 domain of MyBPC. Residue D389 lies in a region of the C2 domain that is highly conserved across mammals (Figure 1B). The IgI–like domain consists of ten β–strands that form two β–sheets (Figure 1C and 1D).

Here, we use correlation–guided enhanced molecular dynamics sampling (CORE–MD II) to study the conformational space of the C2 domain [49–51] (see Materials and Methods for more details). The method relies in part on pa/rtitioning of the entire pathway into short trajectories that we refer to as instances. The CORE–MD II sampling within each instance is accelerated by adaptive path–dependent metadynamics simulations. The second part of the enhanced sampling MD approach involves kinetic Monte Carlo (kMC) sampling between the different configurations that are accessed during each instance. The combination of the partition of the total simulation into short non–equilibrium simulations and the kMC–sampling facilitates the sampling of rare events of protein–dynamics on long time–scales without definitions of *a priori* reaction pathways and additional parameters. Therefore, CORE–MD II enables an acceleration factor of at least 100, as validated by folding simulations of sample peptides [51].

Additionally, we used biochemical approaches to probe the structure, thermostability and protein–protein interactions of the N–terminal domains of MyBPC. In this study, we aim to elucidate the role of the C2 domain and which of the versatile regulatory mechanisms of MyBPC are perturbed by the D389V mutation.

2. Results

2.1 Enhanced CORE–MD II Simulations of the WildTtype and the D389V C2 domain.

We performed enhanced correlation guided CORE–MD II simulations on the C2 wild–type (wt) and the D389V domain for 100 ns each [49–51]. In Figure S1, we display relevant conformers that we extracted from the simulations at different points in time. In the visual analysis of the conformations, we observe that the N–terminal triple β–sheet structure remains relatively stable throughout the simulation in both C2 wt and D389V, whereas the C–terminal region of both proteins exhibits a stronger flexibility and populates a wider conformation range.

We continued with the analysis of the region in proximity to position 389. We determined the free energy landscapes (FEL) as function of the inter–atomic distances between D389 Cγ (wt)/V389Cβ–K395 Nζ and D389 Cγ (wt)/V389Cβ–A417Cα averaged over the

Preprints (www.preprints.org) | NOT PEER-REVIEWED | Posted: 12 October 2021 doi:10.20944/preprints202110.0178.v1

simulation. In Figure 2, we show the FEL of C2 wt and D389V. In the free energy analysis of the wild–type, we find four major minima surrounded by a region that is higher in free energy. The States (1–3) reside at a distance D389–A417 of approximately 1.1 nm, while the State (1) corresponds to the formation of a salt–bridge between D389 and K395 (see Figure 2A). The States (2–3) represent intermediate states. State (4) is defined by a strong interaction of the D389 backbone with both the amino group of K395 and the backbone carbonyl group of the adjacent residue A417.

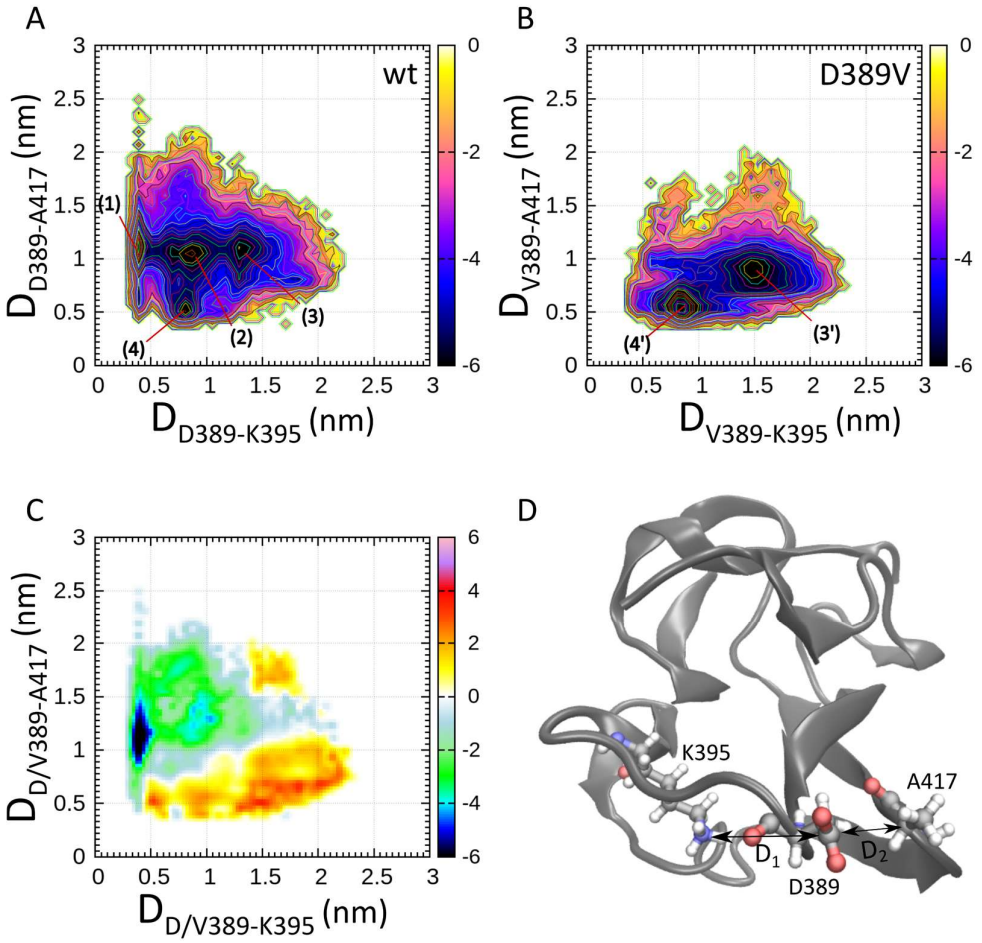

Figure 2. Free Energy Landscapes (FEL) of MyBPC C2 wt (**A**) and D389V (**B**) domains generated using 100 ns of CORE–MD II simulations. The effect of the D389V mutation on the conformational space in vicinity of the mutation is explored. We define the inter–atomic distances between D389V Cγ/V389 Cβ – K395 Nζ and D389V Cγ/V389 Cβ – A417 Cα as principal coordinates of the FEL. The scale of the color bar is given in units of k_BT. (1) – (4) indicate conformational states of C2 wt and (3′) and (4′) those of C2 D389V. (**C**) Difference map of (A) and (B) where negative values indicate an abundance of wt and positive values and abundance of D389V states. (**D**) Sample conformer extracted from State (4) in (A). C2 wt is depicted with the interacting residues D389, K395 and A417. D_1 represents the x–axis and D_2 the y–axis of the distances plotted in figures (A) to (C) for all conformations adapted over the course of the simulation.

A sample conformer of State (4) is displayed in Figure 2D. Looking at the C2 D389V FEL (Figure 2B) or the difference map between C2 wt and D389V (Figure 2C), the common features and differences in conformer population become obvious. State (4) is populated in both wt and D389V protein, which shows that the mutation of the amino acid side chain does not significantly influence the backbone interaction of residue 389 with its partners.

Preprints (www.preprints.org) | NOT PEER-REVIEWED | Posted: 12 October 2021 doi:10.20944/preprints202110.0178.v1

State (3) is also present in both proteins and slightly differs for C2 D389V due to the presence of additional hydrophobic contacts. It is the favorable conformation for C2 D389V, as it features a broad continuum of low energy states around its minimum. In State (3′) of C2 D389V, V389 is closer to A417 and more distant to K395. Predictably, State (1) and State (2) are not populated for C2 D389V, as their emergence relies on the stabilizing effect of the salt–bridge formed between D389 and K395. Hydrophobic interactions between the side chains of V389 and A417 help to bias the conformer dynamics of C2 D389V towards State (3′).

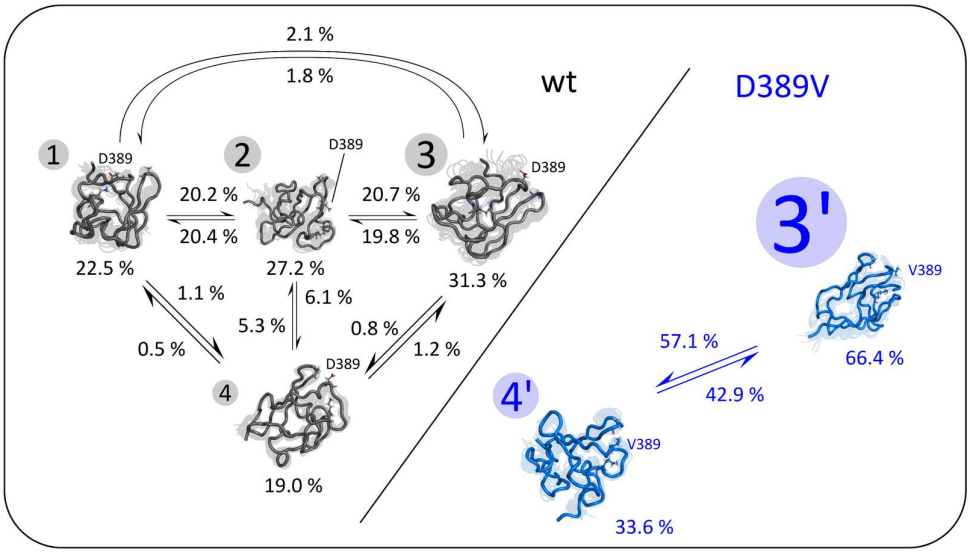

Figure 3. Kinetic network derived from the clustered major conformations of C2 wt and D389V. Representative conformations of the States (1) to (4) identified in Figure 2 are shown for C2 wt (black) and (3′) and (4′) for D389V (blue). Backbone Cα are shown as a tube representation and residues D389, V389, K395 and A417 are shown as CPK model. The opaque underlay displays 40 conformers of each state. The numbers denote the states and their sizes correspond to the relative occupancy of each state over the course of simulation, which is shown below the respective conformers. Arrows and percentages reflect probabilities of transition between two states.

While the FEL analysis revealed that the D389V mutation leads to a shift in the conformational equilibrium and the deletion of States (1–2), it inevitably affects conformational transitions of the C2 domain. We investigated that effect though a kinetic network analysis (see section Material and Methods). Figure 3 shows representative clustered conformations that were selected based on the distances of D389 Cγ or V389 Cβ to K395 Nζ and A417 Cα. In the analysis, we observe that all states share a similar occupancy and State (2) meditates the transition between States (1), (3) and (4). All of these states share the highest transition probabilities with State (2). Apparently, the D389V mutation abolishes the occupancy of States (1) and (2), leading to high prevalence of State (3′) and a slight increase in the population of State (4′). Hence, the local perturbation by mutation D389V appears to have an allosteric effect that involves the occupancy of the energetic states together with the associated kinetic network of state transitions, resulting in a reduction in the overall stability of the C2 domain. [52,53].

To elucidate the effect of D389V on the global conformation of the C2 domain in more detail, we determined time–averaged distance maps for C2 wt and D389V (Figure 4 A and B). Here, the main differences between C2 wt and D389V manifest themselves in relation to the β–strand contacts B4–B5–B6 (β_{4-5-6}) and B1–B6 (β_{1-6} (see Figure 1D). C2 wt exhibits a tight network of interactions involving residues L421–E451 in β_{4-5-6}, while the number of corresponding interactions is substantially reduced in C2 D389V (dotted boxes in Figure 4A and B). In particular, residues L421–D431 are no longer located near residues C436–E441, indicating destabilization or loss of critical β–strand contacts. The structural

Preprints (www.preprints.org) | NOT PEER-REVIEWED | Posted: 12 October 2021 doi:10.20944/preprints202110.0178.v1

consequences of these observations are illustrated in Figure 4C and D for wt and D389V, respectively. A sample conformer of wt protein is shown in grey and D389V in blue with both having residues D430–K450 colored in red. The C–terminal region of C2 wt is predicted to populate a larger ensemble of conformer structures compared to the initial NMR ensemble, where stabilizing interactions remain largely intact. For C2 D389V, residues D430–K450 adopt conformations that have a lower propensity for the formation of contacts $\beta_{4\text{–}5\text{–}6}$. Furthermore, contacts between residues Q401–S406 and residues in proximity of K380 are weakened, while new contacts are established between residues A392–L397 with the N–terminal region. Additionally, the missing salt–bridge interaction destabilizes the interaction of the N–terminal B1 and C–terminal B6 strands, as indicated by the dashed boxes in Figure 4A and B. In summary, the effects implied by CORE–MD II simulations make it likely, that protein thermodynamic properties are altered. We followed this lead by performing the pertinent biochemical experiments.

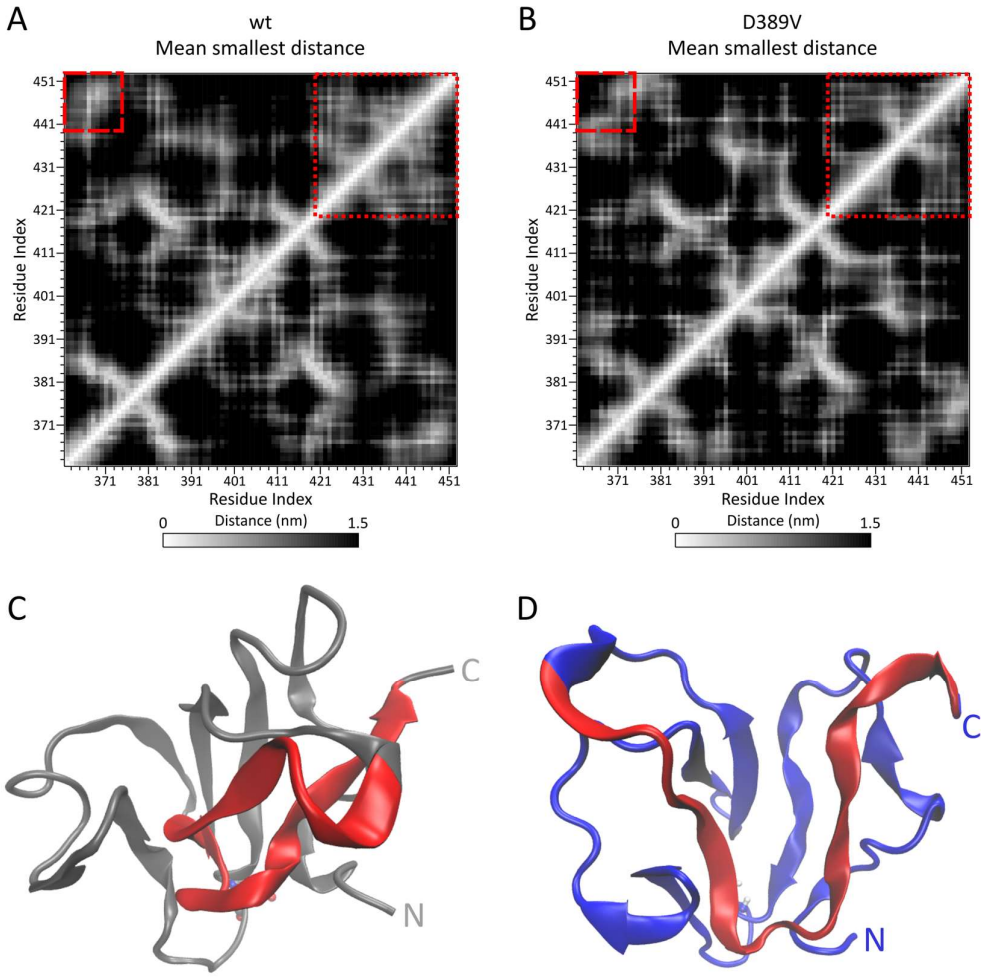

Figure 4. Mean smallest distance matrices for MyBPC C2 wt (**A**) and D389V (**B**). The time–averaged minimum distance of each residue to every other residue is plotted in heat maps with white indicating the smallest and black the largest distance ranging from 0–1.5 nm. This map reveals differences in the global conformational space of C2 wt and D389V. Dotted boxes indicate the β_{456} inter–strand contacts within the C–terminus of the domain. Dashed boxes indicate the β_{16} inter–strand contacts of C2 wt that are destabilized in C2 D389V (for topology see Figure 1D). (**C**) and (**D**) Sample structures of C2 wt (grey) and D389V (blue) to illustrate the differences in C–terminal conformation regarding the dotted boxes in (A) and (B). Residues 430 to 450 are marked in red.

Preprints (www.preprints.org) | NOT PEER-REVIEWED | Posted: 12 October 2021 doi:10.20944/preprints202110.0178.v1

2.2 Structural Integrity and Thermodynamic Stability of N–terminal MyBPC domains

Depending on their position in the protein, point mutations may perturb protein structure by different mechanisms, for example impairment of folding pathways or loss of stabilizing side chain interactions. We performed circular dichroism (CD) experiments to assess the impact of D389V mutation on C2 secondary structure organization. Moreover, we probed C2 domain thermostability using thermal shift assay (TSA) and differential scanning calorimetry (DSC). The relative amount of secondary structure elements as well as melting temperatures in MyBPC C2 and C0–C2 constructs are displayed in Table 1 for wt and D389V, respectively. Spectra of the averaged data for each construct and the thermal unfolding traces are shown each in Figure S2 and Figure S3.

CD spectra show that the C2 wt domain consists of ~35–40% β–sheets and ~30–35%unordered regions with ~10% α–helical and ~20% β–turn content. These data are in good accordance with the published NMR structure [31]. Our CD data indicate no major structural perturbations of the N–terminal domains by the D389V mutation.

Table 1. Structural and thermodynamic analysis of N–terminal MyBPC domains as determined by CD experiments, TSA and DSC. α: α–helix, β: β–sheet, T: turn, U: unordered, Σ: total, T_m: melting temperature. Data are mean ± SEM of at least n=3 experiments.

Construct	α (%)	β (%)	T (%)	U (%)	Σ (%)	T_m (TSA) / °C	T_m (DSC) / °C
C2 wt	7	37	22	34	100	59.3 ± 0.1	56.5 ± 0.3
C2 D389V	7	36	22	35	100	52.1 ± 0.3	52.3 ± 0.2
C0–C2 wt	7	36	24	32	99	51.8 ± 0.5	50.2 ± 0.0
C0–C2 D389V	8	40	22	30	100	48.9 ± 0.6	47.6 ± 0.3

Representative traces of melting curve experiments are shown in Figure S3. The determined T_m values for the C2 wt domain (59.3 ± 0.1 °C in TSA versus 56.5 ± 0.3 °C in DSC) are consistent with the T_m for the MyBPC C4 domain (58 °C), that exhibits the same IgI–like fold as the C2 domain [54]. Interestingly, the mutation also destabilizes the C0–C2 construct, although the T_m of C2 D389V is above that of the C0–C2 wt construct. This suggests that the effect of the mutation propagates throughout the N–terminal domains.

CD, TSA and DSC data indicate a stable fold of all protein constructs. The melting temperature can be interpreted as a measure of protein conformational dynamics. In the native conformation, the protein occupies a local energy minimum and oscillates around that by adopting different conformations. A point mutation can lead to a shift in the conformational distribution, which often decreases thermal stability. The results are consistent with the differences between wt and mutant protein conformations obtained by CORE–MD II simulations. Possible implications for interactions with key sarcomeric proteins such as β–cardiac myosin (β–CM) and α–cardiac actin were further investigated.

2.3 Interaction of N–terminal Domains of MyBPC with Key Sarcomeric Proteins

In order to evaluate binding affinity of MyBPC constructs C2 and C0–C2 to F–actin and synthetic thick filaments of β-cardiac myosin, we performed high–speed co–sedimentation assays. The effect of the interaction of MyBPC with the cardiac thin filament (cTF) has been studied extensively and proposed to tune actomyosin cross–bridge cycling [13,15–17]. MyBPC has further been shown to bind β–CM's regulatory light chain with its N–terminal C0 domain [55] and β–CM S2 with its C0–C2 domains [18,19,56]. Therefore, the extent of altered interaction of MyBPC's N–terminus with cTF or myosin imposed by D389V provides direct implications for cardiac dysregulation.

Preprints (www.preprints.org) | NOT PEER-REVIEWED | Posted: 12 October 2021 doi:10.20944/preprints202110.0178.v1

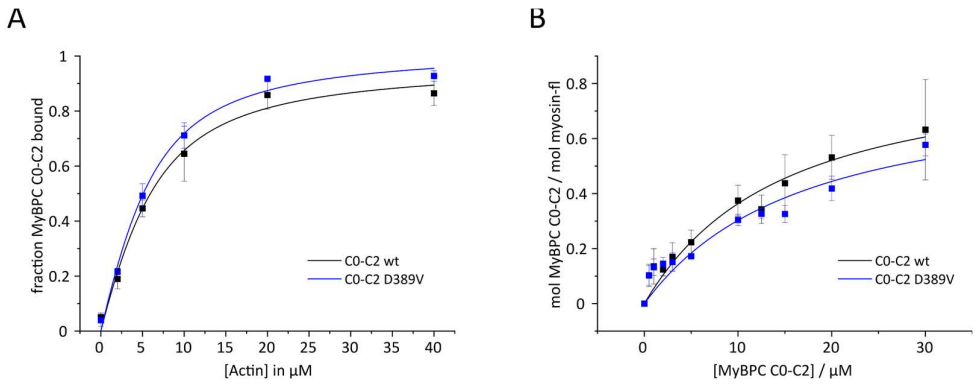

Figure 5. High–speed co–sedimentation experiments of MyBPC C0–C2 with F–actin and β–cardiac myosin. (**A**) 0–40 µM actin and 5 µM MyBPC C0–C2 were co–sedimented and the fraction of C0–C2 in the pellet was determined. A quadratic fit yields the dissociation constants K_d for wt of 3.2 ± 0.9 µM and D389V of 2.8 ± 0.6 µM. (**B**) 0–30 µM MyBPC C0–C2 were co–sedimented with 2.5 µM of β–cardiac myosin. The amount of C0–C2 bound to synthetic thick filaments was determined using a protein standard range of C0–C2. A quadratic fit yields K_d values for wt of 12.7 ± 4.7 µM and D389V of 14.8 ± 7.7 µM. Data points indicate mean ± SD from at least n=3 experiments.

High–speed co–sedimentation probing the affinity of MyBPC C2 to actin or myosin show very weak interaction (Figure S4). Co–sedimentation of 30 µM C2 wt and 40 µM F–actin or 30 µM C2 and 2.5 µM β–cardiac myosin resulted in <2% of C2 in the pellet fraction. Based on these results, a K_d in the range of several 100 µM can be estimated. This very weak binding is consistent with a K_d of 1.1 mM determined for the interaction of C2 with domain S2 of myosin [31].

To assess, whether the D389V mutation affects the binding of other N–terminal domains to myosin and actin, we repeated experiments with MyBPC C0–C2 (Figure 5). The K_d value determined for the interaction of C0–C2 with F–actin of 3.2 ± 0.9 µM is unchanged by the D389V mutation (2.8 ± 0.6 µM). The K_d value of the interaction of myosin with C0–C2 wt has been calculated to be 12.7 ± 4.7 µM, whereas C0–C2 has an affinity of 14.8 ± 7.7 µM. The values are consistent with prior studies [16,18,57,58] and indicate no effect of D389V on the interaction of the N–terminal region of MyBPC with F–actin and myosin.

Since binding of C0–C2 to myosin and F–actin is at least two orders of magnitude stronger, it is unlikely that the interactions of the C2 domain alone are of physiological importance. In fact, several models suggest that the C2 domain in the context of C0–C2 is not in direct contact with F–actin [17] and that a C2–C5 construct does not incorporate into the sarcomere [18].

2.4 Simulation of C2 Domain Unfolding Dynamics

Apart from affecting the equilibrium between myosin DRX and SRX states [19,59–61], MyBPC also regulates contractility in its function as a mechanical tether. MyBPC is C–terminally anchored to the thick filament via its C8–C10 domains. Additional binding of the N–terminal region of MyBPC to the thin filament establishes a mechanical tether that exerts a viscous load during the cross–bridge cycle [26–28,62]. This notion is supported by the fact that in relaxed muscle MyBPC extends from the thick filament toward the thin filament, as demonstrated by the use of electron tomography [63]. Using laser–trap assays, the lifetimes of MyBPC's interaction with the thin filament were determined to range from 20 to 300 ms [28] and therefore outlast actomyosin crossbridges (<200 µs) by at least two orders of magnitude [62,64]. It has been proposed that assuming a 10 nm step of the myosin power stroke upon contraction and antiparallel sliding of the filaments, the force applied to MyBPC increases by 250% [62]. Under the corresponding mechanical strain, it is possible that subdomains between the anchoring points of the both filaments unfold.

Preprints (www.preprints.org) | NOT PEER-REVIEWED | Posted: 12 October 2021 doi:10.20944/preprints202110.0178.v1

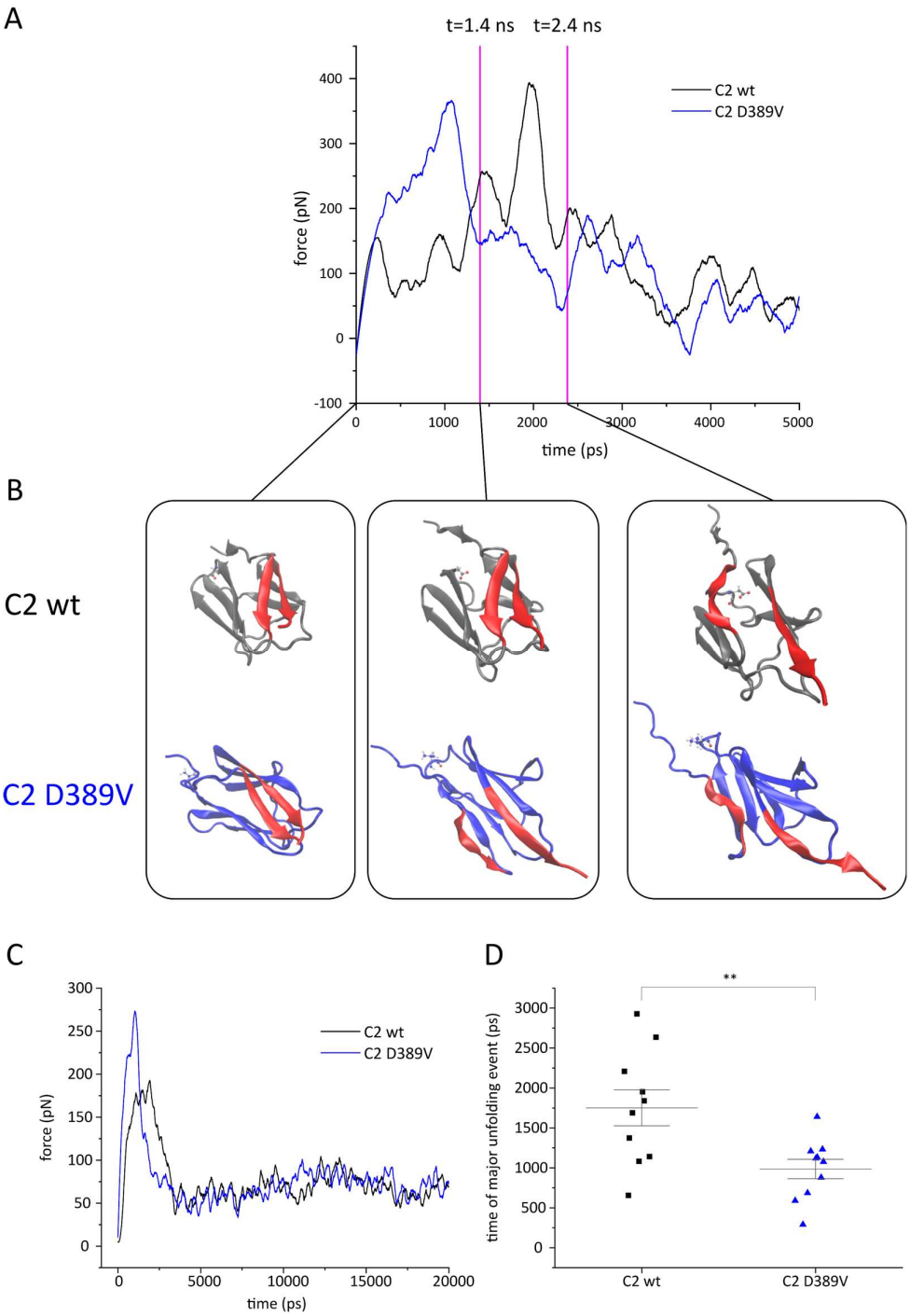

Figure 6. Constant Velocity Steered Molecular Dynamics (cvSMD) simulation of MyBPC C2 domain unfolding. The SMD atom P452Cα was pulled at a velocity of 0.01 Å/ps and the spring constant was set to 7 kcal/mol/Å. (**A**) Sample traces for an unfolding simulation of each wt and D389V MyBPC C2 domain. The force acting on the SMD atom is plotted against the time of the simulation. Data were smoothened using Savitzky–Golay filter to compensate for the noise created by the spring acting on the fixed atom. (**B**) Sample structures of time points 0, 1400 and 2400 ps in the unfolding experiments displayed in (A). C2 wt and C2 D389V are shown in grey and blue, respectively, with residue 389 as a CPK model. Residues A372–K377 and T445–P452 of the parallel β_{16}–strands are marked in red. (**C**) Average of n=10 independent unfolding simulations of each wt and D389V MyBPC C2 domain. The force acting on the SMD atom is plotted against the time of the simulation. Data were smoothened using Savitzky–Golay filter to compensate for the noise created

Preprints (www.preprints.org) | NOT PEER-REVIEWED | Posted: 12 October 2021 doi:10.20944/preprints202110.0178.v1

by the spring acting on the fixed atom. (**D**) The time point of major unfolding event is plotted for each individual unfolding experiment. The major unfolding event is defined as the global maximum of the force–time curve. The peak of unfolding averagely occurred after 1751 ± 714 ps for wt and 986 ± 384 ps for D389V. **: $p < 0.01$

So far, it remains to be determined to what extent the N–terminal domains of MyBPC are contributing to the interaction with F–actin. While neutron scattering data suggest that domains C0 and C1 bind directly to F–actin [17], high–speed co–sedimentation and yeast two–hybrid assays have shown that domains C1 and M are essential for the interaction [16,65]. As C8 is the closest domain attached to the thick filament, the intervening linker domains C2–C7 are predestined to unfold when force is applied during active sarcomere contraction. Using an atomic force microscopy–based approach, this model has been applied to HCM mutations R495W and R502Q in the C3 domain of MyBPC, which shares a similar IgI–like fold with domain C2. The unfolding force as well as the dynamics of unfolding and refolding were examined [62]. Since the C2 domain does not serve as an attachment site on thin filaments, it seems plausible that its function is to act as a brake exerting a set counterforce to cardiac contraction.

To model the mechanical strain to which the C2 domain is subjected, we applied steered molecular dynamics (SMD) simulations [66–68], by pulling on the Cα atom of P452 with constant force while S362Cα remained in place (Figure 6). Example traces of force–time curves are shown in Figure 6A. The maximum counterforce occurs at about 1200 ps for C2 D389V and at 1900 ps for C2 wt. This peak corresponds to the loss of the β_{1-6} inter–strand contacts, as shown in exemplary structures at time points 0, 1400 and 2400 ps in Figure 6B. While the contact β_{1-6} is intact at t=0 in both proteins, it is already broken at t=1400 ps in C2 D389V. The disruption of this structure in C2 wt happens later, after its major peak, as visualized at t=2400 ps. The destabilizing effect of the D389V mutation on the β_{16} contacts has already been demonstrated by the CORE–MD II simulation (Figure 4). A residue matrix view facilitates the comparison between the two simulation methods and illustrates the consistency of the results (Figure S5 and Figure 4).

The averaged force–time curves of ten individual unfolding simulations are shown in Figure 6C. C2 D389V tends to unfold earlier with a sharper force peak and a higher maximum force. The same force is required to unfold C2 wt, but over a broader range of time. This suggests that this part of the C2 D389V structure is more rigid, whereas the C2 wt domain compensates for the applied force by forming various stabilizing contacts during the unfolding process. There were no noticeable differences in the force–time curve for the remaining protein unfolding pathway. Evaluating the time point of the first unfolding peak for every of the ten experiments reveals that the C2 wt unfolding peak occurs after 1751 ± 714 ps and 2–fold faster for C2 D389V at 986 ± 384 ps (Figure 6D). Applying this unfolding mechanism to the MyBPC viscous load model on sarcomeric contraction implicates a different contraction–over–time pattern for carriers of the D389V mutation. Disruption of the finely tuned cardiac contractile cycle provides a molecular basis for the development of HCM. These results provide the basis for further clarification of the pathomechanism underlying the N–terminal part of the *MYBPC3*$^{\Delta 25bp/D389V}$ double mutation.

3. Discussion

Mutations in the *MYBPC3* gene are among the most frequent causes for the development of HCM. Many of them are frameshift mutations that result in the production of truncated protein, which is degraded in the cell, leading to the phenotype of haploinsufficiency [32–37]. In contrast, single amino acid exchanges in MyBPC often alter domain stability or protein–protein interactions, thus exhibiting a poison polypeptide effect [62,69–71].

In this study, we demonstrate that the D389V mutation strongly perturbs the conformational space and the kinetic network of the C2 domain, while leaving the tertiary structure intact. Residue D389 is conserved across many species and isoforms, which appears

Preprints (www.preprints.org) | NOT PEER-REVIEWED | Posted: 12 October 2021 doi:10.20944/preprints202110.0178.v1

to be related to its role in stabilizing the loop structure in which it resides (Figure 1). Four energetic minima were identified by the use of CORE–MD II simulations, involving the interaction of D389 with K395 and A417 (Figures 2 and 3). The D389V mutation abolishes the electrostatic attraction towards K395 and the States (1) and (2) associated with that interaction. Consequently, the kinetic equilibrium of C2 is distorted and State (3) becomes the predominant state in C2 D389V. This allosteric trigger event propagates throughout the whole domain and destabilizes the $\beta_{4–5–6}$ and $\beta_{1–6}$ inter–strand contacts (Figure 4).

The replacement of single amino acids in MyBPC can in some instances disrupt the tertiary structure of the affected domain, as shown for the A31P mutation in the C0 domain [41]. Our CD data suggest that the D389V mutation does not cause a major structural change in the domain structure of the N–terminal constructs C2 and C0–C2 (Table 1 and Figure S2). However, the thermostability of the C2 and C0–C2 domain constructs is decreased by D389V, as demonstrated by TSA and DSC (Table 1), which indicates a different conformational space occupied by these constructs compared to C2 wt constructs. This is in line with the results that were obtained by CORE–MD II simulations.

To fulfill its regulatory roles, MyBPC depends on the interaction of its N–terminus with the key sarcomeric proteins actin and myosin [13,15–19,56]. Our high–speed co–sedimentation data on the isolated C2 domain in interaction with myosin and actin suggest very weak binding (Figure S4), which is consistent with a K_d value of 1.1 mM previously determined for the interaction of C2 with the region containing R870 within subfragment–2 of β–cardiac myosin [31]. The affinities determined for the interaction of C0–C2 with myosin and actin are at least two orders of magnitude greater, which implies that potential interactions of C2 make a minor contribution compared to those of the other N–terminal domains. The values are unchanged by the D389V mutation and consistent with those determined in previous studies [16,18,57,58], thus excluding altered affinities as a pathomechanism.

More recently, the paradigm of MyBPC acting as a mechanical tether, that functions as a brake on cardiac contraction, has come into focus [72]. This idea is supported by observations made by electron tomography, that demonstrated MyBPC spanning from the thick towards the thin filament in relaxed muscle [63]. Studies exposing MyBPC to mechanical strain by the use of atomic force microscopy revealed a structural hierarchy of domain unfolding that is highly conserved across species [26,27]. Our data suggest that C2 is a linker domain that partly unfolds and poses a counterforce upon cardiac contraction. This mechanism has been proposed for the neighboring C3 domain that harbors several HCM–causing mutations [62]. SMD simulations were used to explore potential differences in the unfolding pathways of C2 wt and D389V, by moving the C–terminus and fixing the N–terminus (Figures 6, 7 and S5). The $\beta_{1–6}$ contacts are disrupted twice as fast and with a sharper peak in C2 D389V compared to wt. We also identified the weakening of $\beta_{1–6}$ interaction as a consequence of the D389V mutation upon analysis of the CORE–MD II simulations (Figure 4).

There are several possibilities on how these data relate to the hyperdynamic features observed in *MYBPC3*$^{\Delta 25bp/D389V}$ carriers [48]. The mechanical destabilization of the C2 domain by the D389V mutation results in a reduced capability of MyBPC to apply a counterforce. Moreover, a differential expression of wt and mutant allele across cardiomyocytes—as demonstrated for HCM mutations in *MYH7* [73–75]—could promote an imbalance in contractility of the myocardium. In case the D389V mutation also impairs refolding kinetics, an elevated amount of partly unfolded protein can activate the UPS, which is implicated in HCM [41,76–78].

MyBPC can only exert its tethering function, if it is correctly incorporated into the C–zone of the sarcomere. If 100% of the mRNA transcript originating from *MYBPC3*$^{\Delta 25bp}$ or *MYBPC3*$^{\Delta 25bp/D389V}$ is deprived of exon 33 by alternative splicing, the resulting protein will always have an altered C10 subdomain. That leads to mislocalization of MyBPC to the Z–disc, which has been shown to be sufficient to cause HCM in mice by the pathomechanism of functional haploinsufficiency [47]. This assumption poses two problems. Firstly, func-

Preprints (www.preprints.org) | NOT PEER-REVIEWED | Posted: 12 October 2021 doi:10.20944/preprints202110.0178.v1

tional haploinsufficiency caused by the mislocalised MyBPC^{C10mut} protein would be a potent driver of HCM development in many carriers, as described for several truncation mutations of MyBPC that cause haploinsufficiency [33,36,37]. However, *MYBPC3*$^{\Delta 25bp}$ carriers have an incomplete penetrance in regard to pathogenesis with an odds ratio of 6.99 and develop late–onset HCM [45]. Secondly, *MYBPC3*$^{\Delta 25bp/D389V}$ carriers exhibit increased LVEF, abnormal calcium transients and cardiomyocyte hypertrophy, features not inherent to *MYBPC3*$^{\Delta 25bp}$ carriers [48]. If the D389V mutation does not result in mutant protein incorporated into the sarcomere, there is no plausible molecular mechanism that explains the differences observed between carriers *MYBPC3*$^{\Delta 25bp}$ and *MYBPC3*$^{\Delta 25bp/D389V}$.

The 25 base pair deletion in intron 32 of *MYBPC3*$^{\Delta 25bp}$ and *MYBPC3*$^{\Delta 25bp/D389V}$ has been shown to produce mRNA splice variants that lack exon 33. The probability of this event has been suggested to depend on additional risk factors, such as metabolic syndrome or environmental factors [79]. Moreover, alternative splicing has been shown to be a stochastic process, resulting in a distribution of differently processed mRNA transcripts [80,81]. In fact, this has already been demonstrated for the cardiomyopathy–related gene *LMNA* [82] and *MYBPC3* [83]. For study patients with the *MYBPC3* splice site alteration, newly spliced isoforms were found, although the canonical mRNA sequence was still the predominant one. Furthermore, splicing patterns change as individuals age [84–88].

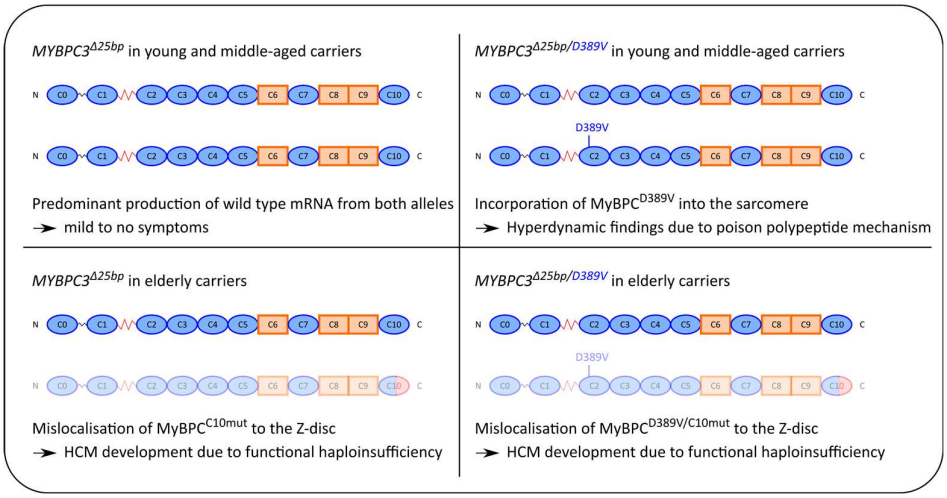

Figure 7: Suggested disease mechanisms as a consequence of age–dependent alternative splicing. All carriers in this model are heterozygous for either of the variants and produce wt protein with at least one allele at any time. Young and middle–aged *MYBPC3*$^{\Delta 25bp}$ carriers predominantly produce wt mRNA from both alleles, yielding mild to no symptoms. For *MYBPC3*$^{\Delta 25bp/D389V}$, this results in the poison polypeptide mechanism and the hyperdynamic findings observed in the patients. Upon ageing, in both *MYBPC3*$^{\Delta 25bp}$ and *MYBPC3*$^{\Delta 25bp/D389V}$ carriers, the alternatively spliced transcript becomes predominant on the allele with the intron deletion, leading to the phenotype of functional haploinsufficiency. The faded representation represents functional haploinsufficiency by mislocalization to the Z–disc.

The consequence of heterozygous *MYBPC3*$^{\Delta 25bp}$ mutation with respect to disease mechanism and the clinical phenotype are schematically depicted in Figure 7. Young carriers exhibit no symptoms or mild conditions because they predominantly produce the wt protein originating from the correctly spliced mRNA. With increasing age, the amount of mutant transcript with skipped exon 33 increases, leading to the production of MyBPC^{C10mut}, which triggers HCM by functional haploinsufficiency [47]. In fact, roughly 90% of *MYBPC3*$^{\Delta 25bp}$ carriers above the age of 60 are symptomatic for HCM [45]. *MYBPC3*$^{\Delta 25bp/D389V}$ carriers produce the protein with a D389V mutation in the C2 domain and an intact C10 domain. The protein localizes to the C–line and exerts its poison polypeptide pathomechanism, as described above. This mechanism corresponds to the clinical

Preprints (www.preprints.org) | NOT PEER-REVIEWED | Posted: 12 October 2021 doi:10.20944/preprints202110.0178.v1

hyperdynamic findings that are found in the *MYBPC3*$^{\Delta 25bp/D389V}$ carriers and that are associated with HCM [48]. With increasing age, as for the *MYBPC3*$^{\Delta 25bp}$ carriers, alternative splicing results in protein production of MyBPC$^{D389V/C10mut}$ that mislocalises to the Z–disc, making functional haploinsufficiency the predominant mechanism.

The genotype–phenotype correlations of MyBPC are very diverse due to the multiplicity of genes and environmental factors influencing the clinical outcome. For example, the occurrence of a *MYH7* mutation in *MYBPC3*$^{\Delta 25bp}$ carriers frequently leads to sudden cardiac death [43]. Extensive genetic screening approaches can discover additional risk factors for genetic variants with an incomplete penetrance for the development of HCM, which has been demonstrated for the *MYBPC3*$^{\Delta 25bp/D389V}$ variant [48]. The pathomechanism largely depends on the ratio of wt to alternatively spliced mRNA transcript originating from the *MYBPC3*$^{\Delta 25bp}$ allele. This question can be addressed by real–time quantitative PCR (qPCR) on tissue biopsies of *MYBPC3*$^{\Delta 25bp}$ and *MYBPC3*$^{\Delta 25bp/D389V}$ carriers using mRNA transcript–specific primers. On the protein level, mass spectrometry can provide information on whether and how much MyBPC^{C10mut} or MyBPC$^{D389V/C10mut}$ protein is produced in the patients. Both of the analysis methods need to include patients of different age, as young *MYBPC3*$^{\Delta 25bp}$ carriers have an incomplete penetrance for HCM, while the prevalence of those over 60 years of age is approximately 90% [45]. Understanding the molecular details in the emergence of this life–threatening disorder will improve predictions about the clinical outcome and enable the development of therapeutic approaches, impacting the lives of millions of carriers.

4. Materials and Methods

4.1 Homology Modeling of the C2 Domain

Homology models of human MyBPC C2 domain were created from an NMR structure of the M and C2 domain (PDB accession code 5k6p [89]) using the software MODELLER [90]. Residues 362–452 of human MyBPC (UniProt Q14896) were aligned to the template using the align2d command. The resulting alignment file served as an input for the AutoModel class, which calculates five 3D models. The model with the highest score was chosen for simulations. The D389V mutation was inserted using the mutator plugin of PyMOL 1.8.6.2 (Schroedinger LLC, USA).

4.2 CORE–MD II Simulation

The CORE–MD II technique is an enhanced MD–simulation method that relies in part on partitioning of the entire pathway into short trajectories that we refer to as instances. The CORE–MD II sampling within each instance is accelerated by adaptive path–dependent metadynamics simulations. The second part of the enhanced sampling MD approach involves kinetic Monte Carlo (kMC) sampling between the different configurations that are accessed during each instance. The combination of the partition of the total simulation into short non–equilibrium simulations and the kMC–sampling facilitates the sampling of rare events of protein–dynamics on long time–scales without definitions of *a priori* reaction pathways and additional parameters.

For the derivation of the CORE–MD II method a global probability $P(x_i(t))$ is defined, that can be sub–divided over N time–slices or subtrajectories k with length τ_k, which are described by local probability densities $\rho_k(x_i(t))$:

$$P(x_i(t)) = \lim_{N\to\infty} \prod_{k}^{N} \rho_k\left(x_i(t)\right) \quad (1)$$

where $x_i(t)$ stands for the coordinate of an atom with the index i.

In the CORE–MD II formalism, we then consider the averaging process of a trajectory dependent quantity $X(t)$, the partition into small trajectories allows for a faster formation of time–averages than the determination of the expectation value of the complete trajectory, which is linked to the time–scale problem of MD–simulations. Therefore, the expectation value of the complete trajectory can be approximated as:

Preprints (www.preprints.org) | NOT PEER-REVIEWED | Posted: 12 October 2021 doi:10.20944/preprints202110.0178.v1

$$\langle X(t)\rangle = X(t)P\big(x_i(t)\big) \approx X(t)\prod_{k}^{K}\rho_k\left(x_i(t)\right) \tag{2}$$

which states that the partition of the complete trajectory into a finite number of K sub–trajectories is approximately sufficient for the sampling of the expectation value $\langle X(t)\rangle$. We define the number of configurations K by a minimal set of the number of atoms N_a in the system, which guarantees a fast forward propagation.

Within each instance k, the local pathway is described by the reduced action $L_{i_k}(t)$:

$$L_{i_k}(t) = \sum_{t<\tau_k} p_i\,(t)\Delta x_i(t) \tag{3}$$

where $\Delta x_i(t) = x_i(t) - \langle x_i(t)\rangle$, $p_i(t)$ is the momentum and t stands for the time. The local path $L_{i_k}(t)$ is used to define the local autocorrelation function $C_{i_k}(t)$:

$$C_{i_k}(t) = \frac{1}{\tau_k}\sum_{t\le\tau_k}\frac{\big(L_{i_k}(t) - \langle L_{i_k}(t)\rangle\big)\big(L_{i_k}(t') - \langle L_{i_k}(t)\rangle\big)}{\big|L_{i_k}(t) - \langle L_{i_k}(t)\rangle\big|\big|L_{i_k}(t') - \langle L_{i_k}(t)\rangle\big|} \tag{4}$$

where $L_{i_k}(t')$ is determined with a frequency equal to 1 ps^{-1} and $\langle\ldots\rangle$ denotes the time–average.

The CORE–MD II [51] technique samples the system along a correlation–dependent probability between states with an index k using a kinetic Monte Carlo (kMC) algorithm. We limit the number of kMC configurations by a minimal set of the number of atoms N_a in the system, which guarantees a fast forward propagation within a small window of three possible selections in each kMC–step.

With a frequency of τ_k, we perform a kMC–step and express a rate r_k for each instance k. We then calculate the cumulative rates and apply the kinetic Monte Carlo algorithm, for the selection of a configuration k with which a configuration is used for the subsequent trajectory instance. The kMC sampling guides the trajectory between equilibrium configurations of the system, where each instance k resembles a state that resides close to the equilibrium state.

We continue with the description of the second component of the CORE–MD II algorithm that applies the local biases. (1) At each initialization of a new trajectory–fragment, the velocities are selected from a random distribution. (2) In order to accelerate the sampling within each instance, we apply a history–dependent bias potential that is related to metadynamics [91], while the history dependency is limited by the time–scale of each instance. We add the Gaussians to the history–dependent potential using the Well–tempered metadynamics technique through a normalization of the added Gaussians by the factor. The corresponding bias is added throughout the simulation.

Finally, we accelerate the sampling within each instance and apply the statistical bias as described in our recent work on the CORE–MD algorithm. We implemented the correlation–dependent bias by a factorization with the variable $\lambda_{i_k}(t)$ with which we scale the gradient of all atoms in the system. This statistical bias enhances the decay of the correlation function and accelerates the access of new states by the system.

For the enhanced MD simulations and the trajectory analysis, we used a modified version of the GROMACS–4.5.5 simulation package [49–51]. For the setup of our simulations, we centered the homology model of the NMR–structure (PDB : 5k6p) in a cubic box with dimensions 5.75 × 5.75 × 5.75 nm^3. For the description of the interactions in the system, we used the AMBER99SB force–field [92,93]. The simulations have been performed in implicit solvent (GBSA), while the electrostatic and van der Waals (vdW) interactions were calculated using a twin–range cut–off 1.2/1.0 nm. The neigborlist with a neighborlist–cutoff equal 1.0 nm was updated every second integration step. The simulations were carried out in the constant–NVT ensemble at a target temperature equal 300 K. For temperature control, we used the Nosé–Hoover thermostat with a coupling constant τ_T equal 1.0 ps.

Preprints (www.preprints.org) | NOT PEER-REVIEWED | Posted: 12 October 2021 doi:10.20944/preprints202110.0178.v1

4.3 MD Trajectory Analysis

In order to define the free energy landscapes (FEL), we projected the free energy on the interatomic distances that we identified as principal coordinates (Distance–definitions). We defined the free energies ΔF using the relation:

$$\Delta F = k_b T \frac{P_i}{P_{min}} \quad (5)$$

Using the same distance definition, we performed a clustering of states with a cutoff of 0.2 nm, in order to determine whether a conformation belongs to a state. We calculated the transition probabilities and the probability for the occurrence of a state using the relative counts of each cluster in relation to the total number of conformations within each state.

4.4 Plasmid Construction

C0–C2 and C2 constructs of MyBPC (UniProt Q14896) with a C–terminal 6xHis–tag were generated from the human full–length cDNA. Gene fragments derived from conventional PCR were inserted between the NdeI and EcoRI sites of pET23a(+). C0–C2 comprises the residues 1–452 and C2 the residues 362–452, consistent with the UniProt entry. D389V variants were generated using site–directed whole plasmid mutagenesis.

4.5 Protein Purification

MyBPC constructs were produced in *Escherichia coli* Rosetta(DE3)pLysS cells. Purification was performed similarly to prior studies [15,16]. MyBPC C2 and C0–2 were affinity–purified using PureCube 100 Ni–NTA Agarose (Cube Biotech, Germany). Protein purity was assessed using SDS–PAGE [94] and protein concentration was determined photometrically using calculated extinction coefficients at 280 nm of 10095 L mol^{-1} cm^{-1} for C2 and 42650 L mol^{-1} cm^{-1} for C0–C2 [95,96]. C2 was subsequently applied to a Superdex 16/600 S75 size exclusion chromatography column (GE Healthcare, USA). C0–C2 was further purified using a HiTrap SP HP 5 ml cation exchange column (Cytiva Life Sciences, USA). Trehalose was supplemented to 10% (w/v), protein aliquots were flash–frozen in liquid N_2 and stored at –80 °C until usage.

β–cardiac myosin from *Sus scrofa* left ventricular tissue was purified essentially as described in [97]. α–cardiac actin was extracted from acetone powder of *Sus scrofa* cardiac tissue according to [98].

4.6 Thermal Stability of MyBPC Subdomains

Protein thermostability was explored in a thermal shift assay (TSA) [99] using SYPRO™ Orange Protein Gel Stain (Thermo Fisher Scientific, USA). C2 was diluted to a concentration of 0.2 mg/mL in a buffer containing 10 mM HEPES pH 7.4, 100 mM NaCl, 1 mM EDTA and 1 mM DTT. C0–C2 was adjusted to 0.5 mg/mL in the same buffer containing 150 mM NaCl. Protein solution was subjected to a temperature gradient of 25 to 80 °C and fluorescence was monitored using a StepOne Real–Time PCR System (Applied Biosystems, USA). Protein melting temperature (T_m) was determined as the midpoint of fluorescence increase.

Differential scanning calorimetry (DSC) was performed using a Nano DSC Model 6300 Differential Scanning Calorimeter (TA Instruments, USA). C0–C2 was diluted to 1.5 mg/mL and C2 to 3.0 mg/mL in the buffers mentioned above. The protein solutions were subjected to a temperature gradient of 25 to 70 °C and the amount of heat required to increase temperature was monitored. The maximum of the acquired curve corresponded to T_m. Data were analyzed using NanoAnalyze software (TA Instruments, USA).

4.7 Circular Dichroism Measurements

Circular Dichroism measurements were performed using PiStar 180 CD spectrometer (Applied Photophysics, United Kingdom). Proteins were diluted into 10 mM NaP_i buffer pH 7.4 with 0.2 mg/ml MyBPC C0–C2, 0.1 mg/ml MyBPC final concentrations. Circular dichroism was recorded as millidegrees for wavelengths from 260 nm to 176 nm with a bandwidth of 4 nm for buffer and protein solutions. Data for each wavelength were

 doi:10.20944/preprints202110.0178.v1

obtained for 10 s and each protein was measured as a triplicate. Data were averaged and buffer subtracted before smoothening using the Savitzky–Golay filter with a polynomial power of 2. Pre–processed data were analyzed using the DichroWeb server [100] and a set of reference spectra for wavelengths from 185 nm to 240 nm [101]. The output of analysis was the mean residue ellipticity for each wavelength as well as the resulting calculated the relative amount of α–helical, β–sheet and unordered regions.

4.6 High–speed Co–Sedimentation Assay

High–speed co–sedimentation assays were used to study protein–protein interactions as described previously [102,103]. G–actin was polymerized for 3 h at room temperature by the addition of $MgCl_2$ to 2 mM and KCl to 100 mM. 0–40 μM F–actin were incubated with 5 μM C0–C2 or 30 μM C2 in 25 mM HEPES pH 7.3, 25 mM KCl, 5 mM $MgCl_2$, 1 mM EGTA and incubated for 30 min at room temperature. Reaction setups were centrifuged for 30 min at 55,000 rpm using a TLA–55 rotor in an Optima TLX Ultracentrifuge (Beckman Coulter, USA). Protein content in supernatant and pellet samples was analyzed using SDS–PAGE and densitometric quantification with Image Lab (Bio–Rad Laboratories, USA)

Synthetic thick filaments of full–length β–cardiac myosin were created by adjusting buffer conditions to 20 mM HEPES pH 7.4, 75 mM NaCl, 2 mM $MgCl_2$, 0.5 mM EDTA, 0.5 mM DTT and incubation on ice for 30 min prior to the experiment. 2.5 μM β–cardiac myosin was incubated with 0–30 μM C0–C2 or C2 for 30 min at room temperature. Centrifugation was performed as above and pellet fractions were analyzed using SDS–PAGE. Amount of protein in the pellet fractions was determined via a protein standard range.

Data analysis was performed using Origin 2020b (OriginLab, USA).

4.8 Steered Molecular Dynamics Simulation

The mechano–stability of C2 was assessed using constant velocity steered molecular dynamics (cvSMD) simulations [66–68] employing NAMD 2.14 [104] with CHARMM36 force fields [105]. The C2 domain was modelled as described above. Temperature was set to 310 K and the GBIS model was used with an alpha–cutoff of 1.2 nm and an ion concentration of 150 mM NaCl. Scaled1–4 was used for non–bonded interactions with a cutoff of 1.4 nm and a switching function at 1.0 nm. A Langevin Nosé–Hoover thermostat was applied with a damping constant of 5.0/ps and hydrogen coupling enabled. Atom restraints were applied to both the fixed and the SMD atom with an exponent for position restraint energy function of 2 and a constraint scaling factor of 1.0. Molecules were equilibrated for 1 ns before performing a 20 ns unfolding simulation. The SMD atom was moved at a constant velocity of 0.01 Å/ps with a force constant of 7 kcal/mol/Å equaling 486.4 pN Å over the course of 20 ns along the vector defined by the way from the fixed to the SMD atom. Results were analyzed by multiplying the force in x, y and z direction acting on the SMD atom with the normalized direction of pulling and plotting the result against the time. Data were smoothened using Savitzky–Golay filter to compensate for the noise created by the spring acting on the fixed atom. Averaged force–time curves consist of ten separate unfolding simulations per construct.

Supplementary Materials: Figure S1: Sample conformers obtained from a 100 ns CORE–MD II simulation of MyBPC C2 wt and D389V domain; Figure S2: Circular Dichroism spectra of MyBPC C2 and C0–C2 domains; Figure S3: Analysis of thermal stability of N–terminal MyBPC constructs; Figure S4: Co–sedimentation assay of MyBPC C2 with F–actin and β–cardiac myosin; Figure S5: Constant Velocity Steered Molecular Dynamics (cvSMD) simulation of MyBPC C2 domain unfolding.

Author Contributions: Conceptualization: F.V.S. and D.J.M.; methodology: F.V.S. purified protein and performed biochemical experiments; F.V.S. and E.K.P. conducted MD simulations and performed the analysis; software: E.K.P. developed the CORE–MD II method used in this study; writing—original draft preparation: F.V.S.; writing—review and editing: F.V.S., M.H.T., E.K.P. and D.J.M.; visualization: F.V.S. and E.K.P.; supervision, M.H.T. and D.J.M.; project administration, funding acquisition: D.J.M. All authors have read and agreed to the published version of the manuscript.

 doi:10.20944/preprints202110.0178.v1

Funding: D.J.M. was supported by Deutsche Forschungsgemeinschaft (DFG) grant MA1081/23–1. D.J.M. is a member of the European Joint Project on Rare Diseases Consortium "PredACTINg" with support from the German Federal Ministry of Education and Research under Grant Agreement 01GM1922B and a member of the Cluster of Excellence RESIST (EXC 2155) with support from the DFG – Project ID 39087428–B11. M.H.T. received support from the Volkswagen Foundation, Joint Lower Saxony – Israeli Research Projects, grant number VWZN3012.

Institutional Review Board Statement: Not applicable.

Informed Consent Statement: Not applicable.

Data Availability Statement: Not applicable.

Acknowledgments: We thank Claudia Thiel for excellent technical assistance. F.V.S. was enrolled in the PhD program Molecular Medicine of Hannover Biomedical Research School (HBRS).

Conflicts of Interest: The authors declare no conflict of interest.

Abbreviations:

Abbreviation	Meaning
β–CM	β–cardiac myosin
CD	Circular Dichroism
cTF	Cardiac thin filament
cvSMD	Constant velocity steered molecular dynamics
DSC	Differential scanning calorimetry
DTT	Dithiothreitol
FEL	Free energy landscapes
GBSA	Generalized Born and surface area continuum solvation
IPTG	Isopropyl β–d–1–thiogalactopyranoside
LVEF	Left ventricular ejection fraction
LVFS	Left ventricular fractional shortening
MyBPC	Cardiac myosin–binding protein C
PBS	Phosphate buffered saline
SDS–PAGE	Sodium dodecyl sulfate polyacrylamide gel electrophoresis
SMD	Steered molecular dynamics
TAME	1,1,1–Tris(aminomethyl)ethane
T_m	Protein melting temperature
TPCK	Tosyl phenylalanyl chloromethyl ketone
TSA	Thermal shift assay
UPS	Ubiquitin proteasome system
vdW	van der Waals
Wt	Wild type

References

1. Semsarian, C.; Ingles, J.; Maron, M.S.; Maron, B.J. New Perspectives on the Prevalence of Hypertrophic Cardiomyopathy. *Journal of the American College of Cardiology* **2015**, *65*, 1249–1254, doi:10.1016/J.JACC.2015.01.019.
2. Maron, B.J.; Maron, M.S. Hypertrophic Cardiomyopathy. *The Lancet* **2013**, *381*, 242–255, doi:10.1016/S0140-6736(12)60397-3.
3. Barsheshet, A.; Brenyo, A.; Moss, A.J.; Goldenberg, I. Genetics of Sudden Cardiac Death. *Curr Cardiol Rep* **2011**, *13*, 364–376, doi:10.1007/s11886-011-0209-y.
4. Wang, L.; Seidman, J.G.; Seidman, C.E. Narrative Review: Harnessing Molecular Genetics for the Diagnosis and Management of Hypertrophic Cardiomyopathy. *Ann Intern Med* **2010**, *152*, 513–520, doi:10.7326/0003-4819-152-8-201004200-00008.

5. Maron, B.J.; Sato, N.; Roberts, W.C.; Edwards, J.E.; Chandra, R.S. Quantitative Analysis of Cardiac Muscle Cell Disorganization in the Ventricular Septum. Comparison of Fetuses and Infants with and without Congenital Heart Disease and Patients with Hypertrophic Cardiomyopathy. *Circulation* **1979**, *60*, 685–696, doi:10.1161/01.cir.60.3.685.
6. Carrier, L.; Mearini, G.; Stathopoulou, K.; Cuello, F. Cardiac Myosin-Binding Protein C (MYBPC3) in Cardiac Pathophysiology. *Gene* **2015**, *573*, 188–197, doi:10.1016/J.GENE.2015.09.008.
7. Heling, L.W.H.J.; Geeves, M.A.; Kad, N.M. MyBP-C: One Protein to Govern Them All. *Journal of Muscle Research and Cell Motility* **2020**, 1–11, doi:10.1007/s10974-019-09567-1.
8. Barefield, D.; Sadayappan, S. Phosphorylation and Function of Cardiac Myosin Binding Protein-C in Health and Disease. *Journal of Molecular and Cellular Cardiology* **2010**, *48*, 866–875, doi:10.1016/j.yjmcc.2009.11.014.
9. Kuster, D.W.D.; Bawazeer, A.C.; Zaremba, R.; Goebel, M.; Boontje, N.M.; van der Velden, J. Cardiac Myosin Binding Protein C Phosphorylation in Cardiac Disease. *J Muscle Res Cell Motil* **2012**, *33*, 43–52, doi:10.1007/s10974-011-9280-7.
10. Freiburg, A.; Gautel, M. A Molecular Map of the Interactions between Titin and Myosin-Binding Protein C. *European Journal of Biochemistry* **1996**, *235*, 317–323, doi:10.1111/j.1432-1033.1996.00317.x.
11. Furst, D.O.; Vinkemeier, U.; Weber, K. Mammalian Skeletal Muscle C-Protein: Purification from Bovine Muscle, Binding to Titin and the Characterization of a Full-Length Human CDNA. *Journal of Cell Science* **1992**, *102*, 769–778, doi:10.1242/jcs.102.4.769.
12. Offer, G.; Moos, C.; Starr, R. A New Protein of the Thick Filaments of Vertebrate Skeletal Myofibrils: Extraction, Purification and Characterization. *Journal of Molecular Biology* **1973**, *74*, 653–676, doi:10.1016/0022-2836(73)90055-7.
13. Flashman, E.; Redwood, C.; Moolman-Smook, J.; Watkins, H. Cardiac Myosin Binding Protein C. *Circulation Research* **2004**, *94*, 1279–1289, doi:10.1161/01.RES.0000127175.21818.C2.
14. Moos, C.; Mason, C.M.; Besterman, J.M.; Feng, I.-N.M.; Dubin, J.H. The Binding of Skeletal Muscle C-Protein to F-Actin, and Its Relation to the Interaction of Actin with Myosin Subfragment-1. *Journal of Molecular Biology* **1978**, *124*, 571–586, doi:10.1016/0022-2836(78)90172-9.
15. Razumova, M.V.; Shaffer, J.F.; Tu, A.-Y.; Flint, G.V.; Regnier, M.; Harris, S.P. Effects of the N-Terminal Domains of Myosin Binding Protein-C in an in Vitro Motility Assay: Evidence for Long-Lived Cross-Bridges. *The Journal of biological chemistry* **2006**, *281*, 35846–54, doi:10.1074/jbc.M606949200.
16. Shaffer, J.F.; Kensler, R.W.; Harris, S.P. The Myosin-Binding Protein C Motif Binds to F-Actin in a Phosphorylation-Sensitive Manner. *Journal of Biological Chemistry* **2009**, *284*, 12318–12327.
17. Whitten, A.E.; Jeffries, C.M.; Harris, S.P.; Trewhella, J. Cardiac Myosin-Binding Protein C Decorates F-Actin: Implications for Cardiac Function. *PNAS* **2008**, *105*, 18360–18365, doi:10.1073/pnas.0808903105.
18. Gruen, M.; Gautel, M. Mutations in β-Myosin S2 That Cause Familial Hypertrophic Cardiomyopathy (FHC) Abolish the Interaction with the Regulatory Domain of Myosin-Binding Protein-C. *Journal of Molecular Biology* **1999**, *286*, 933–949, doi:10.1006/JMBI.1998.2522.
19. Gruen, M.; Prinz, H.; Gautel, M. CAPK-Phosphorylation Controls the Interaction of the Regulatory Domain of Cardiac Myosin Binding Protein C with Myosin-S2 in an on-off Fashion. *FEBS Letters* **1999**, *453*, 254–259, doi:10.1016/S0014-5793(99)00727-9.
20. Starr, R.; Offer, G. The Interaction of C-Protein with Heavy Meromyosin and Subfragment-2. *Biochemical Journal* **1978**, *171*, 813–816, doi:10.1042/bj1710813.
21. McNamara, J.W.; Li, A.; Smith, N.J.; Lal, S.; Graham, R.M.; Kooiker, K.B.; van Dijk, S.J.; Remedios, C.G. dos; Harris, S.P.; Cooke, R. Ablation of Cardiac Myosin Binding Protein-C Disrupts the Super-Relaxed State of Myosin in Murine Cardiomyocytes. *Journal of Molecular and Cellular Cardiology* **2016**, *94*, 65–71, doi:10.1016/j.yjmcc.2016.03.009.
22. McNamara, J.W.; Singh, R.R.; Sadayappan, S. Cardiac Myosin Binding Protein-C Phosphorylation Regulates the Super-Relaxed State of Myosin. *PNAS* **2019**, *116*, 11731–11736, doi:10.1073/pnas.1821660116.

23. Toepfer, C.N.; Wakimoto, H.; Garfinkel, A.C.; McDonough, B.; Liao, D.; Jiang, J.; Tai, A.C.; Gorham, J.M.; Lunde, I.G.; Lun, M.; et al. Hypertrophic Cardiomyopathy Mutations in MYBPC3 Dysregulate Myosin. *Science Translational Medicine* **2019**, *11*, doi:10.1126/scitranslmed.aat1199.
24. Kampourakis, T.; Ponnam, S.; Sun, Y.-B.; Sevrieva, I.; Irving, M.M. Structural and Functional Effects of Myosin-Binding Protein-C Phosphorylation in Heart Muscle Are Not Mimicked by Serine-to-Aspartate Substitutions. *The Journal of biological chemistry* **2018**, *293*, 14270–14275, doi:10.1074/jbc.AC118.004816.
25. Inchingolo, A.V.; Previs, S.B.; Previs, M.J.; Warshaw, D.M.; Kad, N.M. Revealing the Mechanism of How Cardiac Myosin-Binding Protein C N-Terminal Fragments Sensitize Thin Filaments for Myosin Binding. *PNAS* **2019**, *116*, 6828–6835, doi:10.1073/pnas.1816480116.
26. Karsai, Á.; Kellermayer, M.S.Z.; Harris, S.P. Mechanical Unfolding of Cardiac Myosin Binding Protein-C by Atomic Force Microscopy. *Biophysical Journal* **2011**, *101*, 1968–1977, doi:10.1016/j.bpj.2011.08.030.
27. Karsai, Á.; Kellermayer, M.S.Z.; Harris, S.P. Cross-Species Mechanical Fingerprinting of Cardiac Myosin Binding Protein-C. *Biophysical Journal* **2013**, *104*, 2465–2475, doi:10.1016/j.bpj.2013.04.027.
28. Weith, A.; Sadayappan, S.; Gulick, J.; Previs, M.J.; VanBuren, P.; Robbins, J.; Warshaw, D.M. Unique Single Molecule Binding of Cardiac Myosin Binding Protein-C to Actin and Phosphorylation-Dependent Inhibition of Actomyosin Motility Requires 17 Amino Acids of the Motif Domain. *Journal of Molecular and Cellular Cardiology* **2012**, *52*, 219–227, doi:10.1016/J.YJMCC.2011.09.019.
29. Notredame, C.; Higgins, D.G.; Heringa, J. T-Coffee: A Novel Method for Fast and Accurate Multiple Sequence Alignment11Edited by J. Thornton. *Journal of Molecular Biology* **2000**, *302*, 205–217, doi:10.1006/jmbi.2000.4042.
30. Waterhouse, A.M.; Procter, J.B.; Martin, D.M.A.; Clamp, M.; Barton, G.J. Jalview Version 2—a Multiple Sequence Alignment Editor and Analysis Workbench. *Bioinformatics* **2009**, *25*, 1189–1191, doi:10.1093/bioinformatics/btp033.
31. Ababou, A.; Gautel, M.; Pfuhl, M. Dissecting the N-Terminal Myosin Binding Site of Human Cardiac Myosin-Binding Protein C. Structure and Myosin Binding of Domain C2. *The Journal of biological chemistry* **2007**, *282*, 9204–15, doi:10.1074/jbc.M610899200.
32. Helms, A.S.; Thompson, A.D.; Glazier, A.A.; Hafeez, N.; Kabani, S.; Rodriguez, J.; Yob, J.M.; Woolcock, H.; Mazzarotto, F.; Lakdawala, N.K.; et al. Spatial and Functional Distribution of MYBPC3 Pathogenic Variants and Clinical Outcomes in Patients With Hypertrophic Cardiomyopathy. *Circulation: Genomic and Precision Medicine* **2020**, *13*, 396–405, doi:10.1161/CIRCGEN.120.002929.
33. Marston, S.; Copeland, O.; Jacques, A.; Livesey, K.; Tsang, V.; McKenna, W.J.; Jalilzadeh, S.; Carballo, S.; Redwood, C.; Watkins, H. Evidence From Human Myectomy Samples That MYBPC3 Mutations Cause Hypertrophic Cardiomyopathy Through Haploinsufficiency*. *Circulation Research* **2009**, *105*, 219–222, doi:10.1161/CIRCRESAHA.109.202440.
34. O'Leary, T.S.; Snyder, J.; Sadayappan, S.; Day, S.M.; Previs, M.J. MYBPC3 Truncation Mutations Enhance Actomyosin Contractile Mechanics in Human Hypertrophic Cardiomyopathy. *Journal of Molecular and Cellular Cardiology* **2019**, *127*, 165–173, doi:10.1016/j.yjmcc.2018.12.003.
35. van Dijk, S.J.; Dooijes, D.; dos Remedios, C.; Michels, M.; Lamers, J.M.J.; Winegrad, S.; Schlossarek, S.; Carrier, L.; ten Cate, F.J.; Stienen, G.J.M.; et al. Cardiac Myosin-Binding Protein C Mutations and Hypertrophic Cardiomyopathy. *Circulation* **2009**, *119*, 1473–1483, doi:10.1161/CIRCULATIONAHA.108.838672.
36. Barefield, D.; Kumar, M.; Gorham, J.; Seidman, J.G.; Seidman, C.E.; Tombe, P.P. de; Sadayappan, S. Haploinsufficiency of MYBPC3 Exacerbates the Development of Hypertrophic Cardiomyopathy in Heterozygous Mice. *Journal of Molecular and Cellular Cardiology* **2015**, *79*, 234–243, doi:10.1016/j.yjmcc.2014.11.018.
37. Glazier, A.A.; Thompson, A.; Day, S.M. Allelic Imbalance and Haploinsufficiency in MYBPC3-Linked Hypertrophic Cardiomyopathy. *Pflugers Arch - Eur J Physiol* **2019**, *471*, 781–793, doi:10.1007/s00424-018-2226-9.
38. Helms, A.S.; Davis, F.M.; Coleman, D.; Bartolone, S.N.; Glazier, A.A.; Pagani, F.; Yob, J.M.; Sadayappan, S.; Pedersen, E.; Lyons, R.; et al. Sarcomere Mutation-Specific Expression Patterns in Human Hypertrophic Cardiomyopathy. *Circulation: Cardiovascular Genetics* **2014**, *7*, 434–443, doi:10.1161/CIRCGENETICS.113.000448.

39. Nadvi, N.A.; Michie, K.A.; Kwan, A.H.; Guss, J.M.; Trewhella, J. Clinically Linked Mutations in the Central Domains of Cardiac Myosin-Binding Protein C with Distinct Phenotypes Show Differential Structural Effects. *Structure* **2016**, *24*, 105–115, doi:10.1016/j.str.2015.11.001.
40. Bezold, K.L.; Shaffer, J.F.; Khosa, J.K.; Hoye, E.R.; Harris, S.P. A Gain-of-Function Mutation in the M-Domain of Cardiac Myosin-Binding Protein-C Increases Binding to Actin. *The Journal of biological chemistry* **2013**, *288*, 21496–505, doi:10.1074/jbc.M113.474346.
41. Dijk, S.J. van; Kooiker, K.B.; Mazzalupo, S.; Yang, Y.; Kostyukova, A.S.; Mustacich, D.J.; Hoye, E.R.; Stern, J.A.; Kittleson, M.D.; Harris, S.P. The A31P Missense Mutation in Cardiac Myosin Binding Protein C Alters Protein Structure but Does Not Cause Haploinsufficiency. *Archives of biochemistry and biophysics* **2016**, *601*, 133–40, doi:10.1016/j.abb.2016.01.006.
42. Smelter, D.F.; Lange, W.J.D.; Cai, W.; Ge, Y.; Ralphe, J.C. The HCM-Linked W792R Mutation in Cardiac Myosin Binding Protein-C Reduces C6 FnIII Domain Stability. *American Journal of Physiology-Heart and Circulatory Physiology* **2018**, ajpheart.00686.2017, doi:10.1152/ajpheart.00686.2017.
43. Sakthievel, S.; Waldmüller, S.; Saadi, A.; Joseph, P.K.; Rakesh, P.G.; Padmakumar, R.; Jagan M., T.; Richard, P.; Schwartz, K.; Rajamanickam, C.; et al. Novel Mutations in MYH7 and MYBPC3 of an Indian Family Causing Hypertrophic Cardiomyopathy. *Journal of Molecular and Cellular Cardiology* **2001**, *33*, A105, doi:10.1016/S0022-2828(01)90416-X.
44. Waldmüller, S.; Sakthivel, S.; Saadi, A.V.; Selignow, C.; Rakesh, P.G.; Golubenko, M.; Joseph, P.K.; Padmakumar, R.; Richard, P.; Schwartz, K.; et al. Novel Deletions in MYH7 and MYBPC3 Identified in Indian Families with Familial Hypertrophic Cardiomyopathy. *Journal of Molecular and Cellular Cardiology* **2003**, *35*, 623–636, doi:10.1016/S0022-2828(03)00050-6.
45. Dhandapany, P.S.; Sadayappan, S.; Xue, Y.; Powell, G.T.; Rani, D.S.; Nallari, P.; Rai, T.S.; Khullar, M.; Soares, P.; Bahl, A.; et al. A Common MYBPC3 (Cardiac Myosin Binding Protein C) Variant Associated with Cardiomyopathies in South Asia. *Nature genetics* **2009**, *41*, 187–91, doi:10.1038/ng.309.
46. Kuster, D.W.D.; Govindan, S.; Springer, T.I.; Martin, J.L.; Finley, N.L.; Sadayappan, S. A Hypertrophic Cardiomyopathy-Associated MYBPC3 Mutation Common in Populations of South Asian Descent Causes Contractile Dysfunction *. *Journal of Biological Chemistry* **2015**, *290*, 5855–5867, doi:10.1074/jbc.M114.607911.
47. Kuster, D.W.D.; Lynch, T.L.; Barefield, D.Y.; Sivaguru, M.; Kuffel, G.; Zilliox, M.J.; Lee, K.H.; Craig, R.; Namakkal-Soorappan, R.; Sadayappan, S. Altered C10 Domain in Cardiac Myosin Binding Protein-C Results in Hypertrophic Cardiomyopathy. *Cardiovascular Research* **2019**, doi:10.1093/cvr/cvz111.
48. Viswanathan, S.K.; Puckelwartz, M.J.; Mehta, A.; Ramachandra, C.J.A.; Jagadeesan, A.; Fritsche-Danielson, R.; Bhat, R.V.; Wong, P.; Kandoi, S.; Schwanekamp, J.A.; et al. Association of Cardiomyopathy With *MYBPC3* D389V and *MYBPC3* $^{\Delta 25bp}$ Intronic Deletion in South Asian Descendants. *JAMA Cardiology* **2018**, doi:10.1001/jamacardio.2018.0618.
49. Hess, B.; Kutzner, C.; Van Der Spoel, D.; Lindahl, E. GROMACS 4: Algorithms for Highly Efficient, Load-Balanced, and Scalable Molecular Simulation. *Journal of chemical theory and computation* **2008**, *4*, 435–447.
50. Pronk, S.; Páll, S.; Schulz, R.; Larsson, P.; Bjelkmar, P.; Apostolov, R.; Shirts, M.R.; Smith, J.C.; Kasson, P.M.; Van Der Spoel, D. GROMACS 4.5: A High-Throughput and Highly Parallel Open Source Molecular Simulation Toolkit. *Bioinformatics* **2013**, *29*, 845–854.
51. Peter, E.K.; Manstein, D.J.; Shea, J.-E.; Schug, A. CORE-MD II: A Fast, Adaptive, and Accurate Enhanced Sampling Method. *J. Chem. Phys.* **2021**, *155*, 104114, doi:10.1063/5.0063664.
52. Guarnera, E.; Berezovsky, I.N. Toward Comprehensive Allosteric Control over Protein Activity. *Structure* **2019**, *27*, 866-878.e1, doi:10.1016/j.str.2019.01.014.
53. Lu, S.; Shen, Q.; Zhang, J. Allosteric Methods and Their Applications: Facilitating the Discovery of Allosteric Drugs and the Investigation of Allosteric Mechanisms. *Acc. Chem. Res.* **2019**, *52*, 492–500, doi:10.1021/acs.accounts.8b00570.
54. Pricolo, M.R.; Herrero-Galán, E.; Mazzaccara, C.; Losi, M.A.; Alegre-Cebollada, J.; Frisso, G. Protein Thermodynamic Destabilization in the Assessment of Pathogenicity of a Variant of Uncertain Significance in Cardiac Myosin Binding Protein C. *Journal of Cardiovascular Translational Research* **2020**, doi:10.1007/s12265-020-09959-6.

55. Ratti, J.; Rostkova, E.; Gautel, M.; Pfuhl, M. Structure and Interactions of Myosin-Binding Protein C Domain C0: Cardiac-Specific Regulation of Myosin at Its Neck? *The Journal of biological chemistry* **2011**, *286*, 12650–8, doi:10.1074/jbc.M110.156646.
56. Kunst, G.; Kress, K.R.; Gruen, M.; Uttenweiler, D.; Gautel, M.; Fink, R.H.A. Myosin Binding Protein C, a Phosphorylation-Dependent Force Regulator in Muscle That Controls the Attachment of Myosin Heads by Its Interaction With Myosin S2. *Circulation Research* **2000**, *86*, 51–58, doi:10.1161/01.RES.86.1.51.
57. Chow, M.L.; Shaffer, J.F.; Harris, S.P.; Dawson, J.F. Altered Interactions between Cardiac Myosin Binding Protein-c and α-Cardiac Actin Variants Associated with Cardiomyopathies. *Archives of Biochemistry and Biophysics* **2014**, *550–551*, 28–32, doi:10.1016/j.abb.2014.04.003.
58. Singh, R.R.; McNamara, J.W.; Sadayappan, S. Mutations in Myosin S2 Alter Cardiac Myosin-Binding Protein-C Interaction in Hypertrophic Cardiomyopathy in a Phosphorylation-Dependent Manner. *Journal of Biological Chemistry* **2021**, *297*, 100836, doi:10.1016/j.jbc.2021.100836.
59. Calaghan, S.C.; Trinick, J.; Knight, P.J.; White, E. A Role for C-Protein in the Regulation of Contraction and Intracellular Ca2+ in Intact Rat Ventricular Myocytes. *The Journal of Physiology* **2000**, *528*, 151–156, doi:10.1111/j.1469-7793.2000.00151.x.
60. Colson, B.A.; Bekyarova, T.; Locher, M.R.; Fitzsimons, D.P.; Irving, T.C.; Moss, R.L. Protein Kinase A–Mediated Phosphorylation of CMyBP-C Increases Proximity of Myosin Heads to Actin in Resting Myocardium. *Circulation Research* **2008**, *103*, 244–251, doi:10.1161/CIRCRESAHA.108.178996.
61. Kensler, R.W.; Craig, R.; Moss, R.L. Phosphorylation of Cardiac Myosin Binding Protein C Releases Myosin Heads from the Surface of Cardiac Thick Filaments. *Proceedings of the National Academy of Sciences of the United States of America* **2017**, *114*, E1355–E1364, doi:10.1073/pnas.1614020114.
62. Suay-Corredera, C.; Pricolo, M.R.; Velázquez-Carreras, D.; Pathak, D.; Nandwani, N.; Pimenta-Lopes, C.; Sánchez-Ortiz, D.; Urrutia-Irazabal, I.; Vilches, S.; Dominguez, F.; et al. Nanomechanical Phenotypes in Cardiac Myosin-Binding Protein C Mutants That Cause Hypertrophic Cardiomyopathy. *ACS Nano* **2021**, doi:10.1021/acsnano.1c02242.
63. Luther, P.K.; Winkler, H.; Taylor, K.; Zoghbi, M.E.; Craig, R.; Padrón, R.; Squire, J.M.; Liu, J. Direct Visualization of Myosin-Binding Protein C Bridging Myosin and Actin Filaments in Intact Muscle. *PNAS* **2011**, *108*, 11423–11428, doi:10.1073/pnas.1103216108.
64. Woody; Winkelmann, D.A.; Capitanio, M.; Ostap, E.M.; Goldman, Y.E. Single Molecule Mechanics Resolves the Earliest Events in Force Generation by Cardiac Myosin. *eLife* **2019**, *8*, e49266, doi:10.7554/eLife.49266.
65. Bhuiyan, Md.S.; Gulick, J.; Osinska, H.; Gupta, M.; Robbins, J. Determination of the Critical Residues Responsible for Cardiac Myosin Binding Protein C's Interactions. *Journal of Molecular and Cellular Cardiology* **2012**, *53*, 838–847, doi:10.1016/j.yjmcc.2012.08.028.
66. Isralewitz, B.; Gao, M.; Schulten, K. Steered Molecular Dynamics and Mechanical Functions of Proteins. *Current Opinion in Structural Biology* **2001**, *11*, 224–230, doi:10.1016/S0959-440X(00)00194-9.
67. Izrailev, S.; Stepaniants, S.; Isralewitz, B.; Kosztin, D.; Lu, H.; Molnar, F.; Wriggers, W.; Schulten, K. Steered Molecular Dynamics. In Proceedings of the Computational Molecular Dynamics: Challenges, Methods, Ideas; Deuflhard, P., Hermans, J., Leimkuhler, B., Mark, A.E., Reich, S., Skeel, R.D., Eds.; Springer: Berlin, Heidelberg, 1999; pp. 39–65.
68. Lu, H.; Isralewitz, B.; Krammer, A.; Vogel, V.; Schulten, K. Unfolding of Titin Immunoglobulin Domains by Steered Molecular Dynamics Simulation. *Biophysical Journal* **1998**, *75*, 662–671, doi:10.1016/S0006-3495(98)77556-3.
69. Da'as, S.I.; Fakhro, K.; Thanassoulas, A.; Krishnamoorthy, N.; Saleh, A.; Calver, B.L.; Safieh-Garabedian, B.; Toft, E.; Nounesis, G.; Lai, F.A.; et al. Hypertrophic Cardiomyopathy-Linked Variants of Cardiac Myosin-Binding Protein C3 Display Altered Molecular Properties and Actin Interaction. *Biochemical Journal* **2018**, *475*, 3933–3948, doi:10.1042/BCJ20180685.
70. Doh, C.Y.; Li, J.; Mamidi, R.; Stelzer, J. The HCM-Causing Y235S CMyBPC Mutation Accelerates Contractile Function by Altering C1 Domain Structure. *Biochimica et Biophysica Acta (BBA) - Molecular Basis of Disease* **2019**, doi:10.1016/j.bbadis.2019.01.007.

71. Li, R.H.L.; Stern, J.A.; Ho, V.; Tablin, F.; Harris, S.P. Platelet Activation and Clopidogrel Effects on ADP-Induced Platelet Activation in Cats with or without the A31P Mutation in MYBPC3. *Journal of Veterinary Internal Medicine* **2016**, *30*, 1619–1629, doi:10.1111/jvim.14568.
72. Previs, M.J.; Previs, S.B.; Gulick, J.; Robbins, J.; Warshaw, D.M. Molecular Mechanics of Cardiac Myosin-Binding Protein C in Native Thick Filaments. *Science* **2012**, *337*, 1215–1218, doi:10.1126/science.1223602.
73. Brenner, B.; Seebohm, B.; Tripathi, S.; Montag, J.; Kraft, T. Familial Hypertrophic Cardiomyopathy: Functional Variance among Individual Cardiomyocytes as a Trigger of FHC-Phenotype Development. *Front. Physiol.* **2014**, *0*, doi:10.3389/fphys.2014.00392.
74. Kraft, T.; Montag, J.; Radocaj, A.; Brenner, B. Hypertrophic Cardiomyopathy. *Circulation Research* **2016**, *119*, 992–995, doi:10.1161/CIRCRESAHA.116.309804.
75. Kraft, T.; Montag, J. Altered Force Generation and Cell-to-Cell Contractile Imbalance in Hypertrophic Cardiomyopathy. *Pflugers Arch - Eur J Physiol* **2019**, *471*, 719–733, doi:10.1007/s00424-019-02260-9.
76. Chen, B.; Retzlaff, M.; Roos, T.; Frydman, J. Cellular Strategies of Protein Quality Control. *Cold Spring Harb Perspect Biol* **2011**, *3*, a004374, doi:10.1101/cshperspect.a004374.
77. Predmore, J.M.; Wang, P.; Davis, F.; Bartolone, S.; Westfall, M.V.; Dyke, D.B.; Pagani, F.; Powell, S.R.; Day, S.M. Ubiquitin Proteasome Dysfunction in Human Hypertrophic and Dilated Cardiomyopathies. *Circulation* **2010**, *121*, 997–1004, doi:10.1161/CIRCULATIONAHA.109.904557.
78. Wang, L.; Lai, G.; Chu, G.; Liang, X.; Zhao, Y. CMyBP-C Was Decreased via KLHL3-Mediated Proteasomal Degradation in Congenital Heart Diseases. *Experimental Cell Research* **2017**, *355*, 18–25, doi:10.1016/j.yexcr.2017.03.025.
79. Sadayappan, S.; Puckelwartz, M.J.; McNally, E.M. South Asian–Specific MYBPC3Δ25bp Intronic Deletion and Its Role in Cardiomyopathies and Heart Failure. *Circulation: Genomic and Precision Medicine* **2020**, *13*, e002986, doi:10.1161/CIRCGEN.120.002986.
80. Blencowe, B.J. Alternative Splicing: New Insights from Global Analyses. *Cell* **2006**, *126*, 37–47, doi:10.1016/j.cell.2006.06.023.
81. Melamud, E.; Moult, J. Stochastic Noise in Splicing Machinery. *Nucleic Acids Research* **2009**, *37*, 4873–4886, doi:10.1093/nar/gkp471.
82. Ito, K.; Patel, P.N.; Gorham, J.M.; McDonough, B.; DePalma, S.R.; Adler, E.E.; Lam, L.; MacRae, C.A.; Mohiuddin, S.M.; Fatkin, D.; et al. Identification of Pathogenic Gene Mutations in LMNA and MYBPC3 That Alter RNA Splicing. *PNAS* **2017**, *114*, 7689–7694, doi:10.1073/pnas.1707741114.
83. Dainis, A.; Tseng, E.; Clark, T.A.; Hon, T.; Wheeler, M.; Ashley, E. Targeted Long-Read RNA Sequencing Demonstrates Transcriptional Diversity Driven by Splice-Site Variation in MYBPC3. *Circulation: Genomic and Precision Medicine* **2019**, *12*, e002464, doi:10.1161/CIRCGEN.119.002464.
84. Holly, A.C.; Melzer, D.; Pilling, L.C.; Fellows, A.C.; Tanaka, T.; Ferrucci, L.; Harries, L.W. Changes in Splicing Factor Expression Are Associated with Advancing Age in Man. *Mechanisms of Ageing and Development* **2013**, *134*, 356–366, doi:10.1016/j.mad.2013.05.006.
85. Latorre, E.; Harries, Lorna.W. Splicing Regulatory Factors, Ageing and Age-Related Disease. *Ageing Research Reviews* **2017**, *36*, 165–170, doi:10.1016/j.arr.2017.04.004.
86. Li, H.; Wang, Z.; Ma, T.; Wei, G.; Ni, T. Alternative Splicing in Aging and Age-Related Diseases. *Translational Medicine of Aging* **2017**, *1*, 32–40, doi:10.1016/j.tma.2017.09.005.
87. Roux, J.; Robinson-Rechavi, M. Age-Dependent Gain of Alternative Splice Forms and Biased Duplication Explain the Relation between Splicing and Duplication. *Genome Res.* **2011**, *21*, 357–363, doi:10.1101/gr.113803.110.
88. Wang, K.; Wu, D.; Zhang, H.; Das, A.; Basu, M.; Malin, J.; Cao, K.; Hannenhalli, S. Comprehensive Map of Age-Associated Splicing Changes across Human Tissues and Their Contributions to Age-Associated Diseases. *Sci Rep* **2018**, *8*, 10929, doi:10.1038/s41598-018-29086-2.
89. Michie, K.A.; Kwan, A.H.; Tung, C.-S.; Guss, J.M.; Trewhella, J. A Highly Conserved Yet Flexible Linker Is Part of a Polymorphic Protein-Binding Domain in Myosin-Binding Protein C. *Structure (London, England : 1993)* **2016**, *24*, 2000–2007, doi:10.1016/j.str.2016.08.018.

90. Šali, A.; Blundell, T.L. Comparative Protein Modelling by Satisfaction of Spatial Restraints. *Journal of Molecular Biology* **1993**, *234*, 779–815, doi:10.1006/jmbi.1993.1626.
91. Laio, A.; Parrinello, M. Escaping Free-Energy Minima. *PNAS* **2002**, *99*, 12562–12566, doi:10.1073/pnas.202427399.
92. Hornak, V.; Abel, R.; Okur, A.; Strockbine, B.; Roitberg, A.; Simmerling, C. Comparison of Multiple Amber Force Fields and Development of Improved Protein Backbone Parameters. *Proteins: Structure, Function, and Bioinformatics* **2006**, *65*, 712–725.
93. Kollman, P.A. Advances and Continuing Challenges in Achieving Realistic and Predictive Simulations of the Properties of Organic and Biological Molecules. *Acc. Chem. Res.* **1996**, *29*, 461–469, doi:10.1021/ar9500675.
94. Laemmli, U.K. Cleavage of Structural Proteins during the Assembly of the Head of Bacteriophage T4. *Nature* **1970**, *227*, 680–685, doi:10.1038/227680a0.
95. Gasteiger, E.; Gattiker, A.; Hoogland, C.; Ivanyi, I.; Appel, R.D.; Bairoch, A. ExPASy: The Proteomics Server for in-Depth Protein Knowledge and Analysis. *Nucleic Acids Research* **2003**, *31*, 3784–3788, doi:10.1093/nar/gkg563.
96. Gasteiger, E.; Hoogland, C.; Gattiker, A.; Duvaud, S.; Wilkins, M.R.; Appel, R.D.; Bairoch, A. Protein Identification and Analysis Tools on the ExPASy Server. *The Proteomics Protocols Handbook* **2005**, 571–607, doi:10.1385/1-59259-890-0:571.
97. Margossian, S.S.; Lowey, S. [7] Preparation of Myosin and Its Subfragments from Rabbit Skeletal Muscle. *Methods in Enzymology* **1982**, *85*, 55–71, doi:10.1016/0076-6879(82)85009-X.
98. Lehrer, S.S.; Kerwar, G. Intrinsic Fluorescence of Actin. *Biochemistry* **1972**, *11*, 1211–1217, doi:10.1021/bi00757a015.
99. Lo, M.-C.; Aulabaugh, A.; Jin, G.; Cowling, R.; Bard, J.; Malamas, M.; Ellestad, G. Evaluation of Fluorescence-Based Thermal Shift Assays for Hit Identification in Drug Discovery. *Analytical Biochemistry* **2004**, *332*, 153–159, doi:10.1016/j.ab.2004.04.031.
100. Lobley, A.; Whitmore, L.; Wallace, B.A. DICHROWEB: An Interactive Website for the Analysis of Protein Secondary Structure from Circular Dichroism Spectra. *Bioinformatics* **2002**, *18*, 211–212.
101. Sreerama, N.; Woody, R.W. Estimation of Protein Secondary Structure from Circular Dichroism Spectra: Comparison of CONTIN, SELCON, and CDSSTR Methods with an Expanded Reference Set. *Analytical Biochemistry* **2000**, *287*, 252–260, doi:10.1006/abio.2000.4880.
102. Taft, M.H.; Behrmann, E.; Munske-Weidemann, L.-C.; Thiel, C.; Raunser, S.; Manstein, D.J. Functional Characterization of Human Myosin-18A and Its Interaction with F-Actin and GOLPH3 *. *Journal of Biological Chemistry* **2013**, *288*, 30029–30041, doi:10.1074/jbc.M113.497180.
103. Latham, S.L.; Weiß, N.; Schwanke, K.; Thiel, C.; Croucher, D.R.; Zweigerdt, R.; Manstein, D.J.; Taft, M.H. Myosin-18B Regulates Higher-Order Organization of the Cardiac Sarcomere through Thin Filament Cross-Linking and Thick Filament Dynamics. *Cell Reports* **2020**, *32*, 108090, doi:10.1016/j.celrep.2020.108090.
104. Phillips, J.C.; Hardy, D.J.; Maia, J.D.C.; Stone, J.E.; Ribeiro, J.V.; Bernardi, R.C.; Buch, R.; Fiorin, G.; Hénin, J.; Jiang, W.; et al. Scalable Molecular Dynamics on CPU and GPU Architectures with NAMD. *J. Chem. Phys.* **2020**, *153*, 044130, doi:10.1063/5.0014475.
105. Huang, J.; MacKerell, A.D. CHARMM36 All-Atom Additive Protein Force Field: Validation Based on Comparison to NMR Data. *Journal of Computational Chemistry* **2013**, *34*, 2135–2145, doi:10.1002/jcc.23354.